Monthly Notices
of the
ROYAL ASTRONOMICAL SOCIETY

MNRAS **432,** 3005–3024 (2013)
Advance Access publication 2013 May 27

doi:10.1093/mnras/stt649

Enriching the hot circumgalactic medium

Robert A. Crain,[1]⋆ Ian G. McCarthy,[2,3] Joop Schaye,[1] Tom Theuns[4,5] and Carlos S. Frenk[4]

[1]*Leiden Observatory, Leiden University, PO Box 9513, NL-2300 RA Leiden, the Netherlands*
[2]*Astrophysics and Space Research Group, School of Physics and Astronomy, University of Birmingham, Edgbaston, Birmingham B15 2TT, UK*
[3]*Astrophysics Research Institute, Liverpool John Moores Unviersity, Birkenhead CH41 1LD, UK*
[4]*Institute for Computational Cosmology, Department of Physics, University of Durham, South Road, Durham DH1 3LE, UK*
[5]*Department of Physics, University of Antwerp, Campus Groenenborger, Groenenborgerlaan 171, B-2020 Antwerp, Belgium*

Accepted 2013 April 16. Received 2013 April 15; in original form 2012 May 25

ABSTRACT

Simple models of galaxy formation in a cold dark matter universe predict that massive galaxies are surrounded by a hot, quasi-hydrostatic circumgalactic corona of slowly cooling gas, predominantly accreted from the intergalactic medium (IGM). This prediction is borne out by the recent cosmological hydrodynamical simulations of Crain et al., which reproduce observed scaling relations between the X-ray and optical properties of nearby disc galaxies. Such coronae are metal poor, but observations of the X-ray emitting circumgalactic medium (CGM) of local galaxies typically indicate enrichment to near-solar iron abundance, potentially signalling a shortcoming in current models of galaxy formation. We show here that, while the hot CGM of galaxies formed in the simulations is typically metal poor in a mass-weighted sense, its X-ray luminosity-weighted metallicity is often close to solar. This bias arises because the soft X-ray emissivity of a typical ∼0.1 keV corona is dominated by collisionally excited metal ions that are synthesized in stars and recycled into the hot CGM. We find that these metals are ejected primarily by stars that form in situ to the main progenitor of the galaxy, rather than in satellites or external galaxies. The enrichment of the hot CGM therefore proceeds in an 'inside–out' fashion throughout the assembly of the galaxy: metals are transported from the central galaxy by supernova-driven winds and convection over several Gyr, establishing a strong negative radial metallicity gradient. Whilst metal ions synthesized by stars are necessary to produce the X-ray emissivity that enables the hot CGM of isolated galaxies to be detected with current instrumentation, the electrons that collisionally excite them are equally important. Since our simulations indicate that the electron density of hot coronae is dominated by the metal-poor gas accreted from the IGM, we infer that the hot CGM observed via X-ray emission is the outcome of both hierarchical accretion and stellar recycling.

Key words: galaxies: formation – galaxies: haloes – intergalactic medium.

1 INTRODUCTION

Circumgalactic coronae in quasi-hydrostatic equilibrium around massive galaxies, formed by the accretion and shock heating of intergalactic gas, are a simple but fundamental prediction of galaxy formation models in a cold dark matter (CDM) universe (White & Frenk 1991; Kauffmann, White & Guiderdoni 1993; Cole et al. 2000; Hatton et al. 2003; Bower et al. 2006; Croton et al. 2006; Monaco, Fontanot & Taffoni 2007; Somerville et al. 2008; Benson 2010). Their properties were first explored analytically by White & Frenk (1991, hereafter WF91), who posited that coronae associated with $L_\star$ galaxies at $z = 0$ have temperatures of $T \sim 10^6$ K, and emit $\sim 10^{41}$–10^{43} erg s^{-1} of cooling radiation, primarily in the form of soft (∼0.1 keV) X-ray photons. If present in the local Universe, circumgalactic reservoirs of this luminosity should have been detected, if not by previous generations of X-ray satellites, certainly by *Chandra* and *XMM–Newton*.

The well-documented failure of the *Einstein* and *ROSAT* X-ray observatories to detect hot atmospheres associated with massive disc galaxies (e.g. Bregman & Glassgold 1982; Vogler, Pietsch & Kahabka 1995; Bregman & Houck 1997; Fabbiano & Juda 1997; Benson et al. 2000) has often been regarded as a fundamental challenge to galaxy formation theory. More recently, the greater sensitivity of the *Chandra* and *XMM–Newton* observatories has led to detections of a hot circumgalactic medium (CGM) associated

⋆ E-mail: crain@strw.leidenuniv.nl

with both isolated disc galaxies (Strickland et al. 2004; Wang 2005; Tüllmann et al. 2006; Li, Wang & Hameed 2007; Jeltema, Binder & Mulchaey 2008; Owen & Warwick 2009; Rasmussen et al. 2009; Sun et al. 2009; Li et al. 2011) and isolated elliptical galaxies, with no obvious signature of a contribution from active galactic nuclei (AGN; David et al. 2006; Mulchaey & Jeltema 2010). However, these data have not established the validity of the canonical galaxy formation framework because the inferred X-ray luminosity is typically one to two orders of magnitude fainter than that predicted by analytic models. Moreover, the origin of the hot gas in these examples remains controversial.

Most commonly, extraplanar X-ray emission associated with disc galaxies is interpreted as a signature of hot ejecta from Type II supernovae (SNe) entrained in galaxy-wide outflows. Prima facie, this interpretation is not without merit since several studies report a correlation between the extraplanar X-ray luminosity ($L_{\rm X}$) and star formation indicators such as Hα line emission or broad-band optical/infrared (IR) luminosity (e.g. Rasmussen, Stevens & Ponman 2004; Strickland et al. 2004; Tüllmann et al. 2006; Sun et al. 2007; Li & Wang 2013). Particularly, spectacular cases such as the archetypal local starburst system, M82, bolster this interpretation because of the biconical morphology of their X-ray surface brightness contours and the presence of coincident optical line emission (Strickland et al. 2004; Veilleux, Cecil & Bland-Hawthorn 2005).

In contrast to disc galaxies, the association of hot circumgalactic gas with elliptical galaxies has been established for many years (e.g. Forman et al. 1979; Forman, Jones & Tucker 1985; Fabbiano 1989). In common with disc galaxies, however, the hot gas is commonly interpreted as having an internal origin[1] as the ejecta associated with evolved stellar populations such as Type Ia SNe and asymptotic giant branch (AGB) stars (see e.g. Mathews 1990; Ciotti et al. 1991; Mathews & Brighenti 2003; Parriott & Bregman 2008). This interpretation seems reasonable because evolved stellar populations unquestionably return a significant mass of gas to the interstellar medium (ISM) when integrated over the lifetime of the galaxy. Moreover, a broad correlation between $L_{\rm X}$ and the stellar mass of the galaxy ($M_\star$, or proxies such as $L_{\rm K}$) has now been firmly established in deep *Chandra* observations after careful removal of contaminating X-ray sources (Boroson, Kim & Fabbiano 2011).

The interpretation of diffuse X-ray emission as a signature of internal, stellar processes, rather than an accreted coronal reservoir, therefore, presents a challenge to current models of galaxy formation. Motivated by this challenge, we conducted a study (Crain et al. 2010, hereafter Paper I) using the cosmological hydrodynamic simulations of the Galaxies–Intergalactic Medium Interaction Calculation (GIMIC; Crain et al. 2009, hereafter C09) to investigate the origin and nature of the hot CGM associated with an unprecedentedly large sample of $\sim$500$L_\star$ simulated galaxies. Our analysis demonstrated that M82-like systems, whose X-ray luminosity is dominated by hot gas entrained in outflows, are indeed found in the GIMIC simulations. However, just as in the local Universe, such systems are rare. The majority of $\sim L_\star$ galaxies instead develop extended, quasi-hydrostatic coronae, primarily through the shock heating and adiabatic compression of gas accreted from the intergalactic medium (IGM), supplemented by relatively small amounts of gas recycled through the galaxy by stellar evolution processes.

This picture appears similar to that posited by the analytic model of WF91 but, crucially, the X-ray luminosity of the hot CGM of GIMIC galaxies is one to two orders of magnitude fainter (at fixed halo mass) than that predicted by WF91. The more detailed and accurate treatment of gas accretion and feedback in the GIMIC simulations highlights that the discrepancy stems primarily from inaccurate assumptions regarding the physical structure of the corona adopted by WF91. The X-ray luminosity of GIMIC galaxies is therefore broadly consistent with measurements inferred from *Chandra* and *XMM–Newton* observations of local galaxies. For example, Anderson & Bregman (2011) and Dai et al. (2012) recently reported detections of luminous coronae associated with the giant disc galaxies NGC 1961 and UGC 12591, respectively, whose inferred coronal luminosities correspond closely with those of similarly massive disc galaxies in GIMIC.

It was noted in Paper I that GIMIC galaxies exhibit a tight correlation between $L_{\rm X}$ and halo mass (M_{200}), and this naturally gives rise to a broad correlation between $L_{\rm X}$ and both stellar mass ($M_\star$) and the star formation rate ($\dot{M}_\star$) since, to first order, both of these quantities correlate with M_{200}. Hence, these observed correlations do not necessarily imply an internal origin for the hot gas. This raises the appealing possibility of unifying the interpretation of X-ray observations of disc and elliptical galaxies in a simple model in which, as is inferred in all cosmologically motivated models of galaxy formation, the CGM of galaxies is established by a mixture of intergalactic gas accreted throughout their assembly history and small amounts of internally recycled gas.

We intend to explore such a unification in detail elsewhere, and focus here on what has long been perceived as a problem for the canonical galaxy formation framework: that the hot CGM of $\sim L_\star$ elliptical galaxies appears to be enriched to a significant fraction of the solar metallicity.[2] Such high metallicities were first revealed by high spectral resolution X-ray spectroscopy of NGC 4636 (Xu et al. 2002) and NGC 5044 (Tamura et al. 2003) using *XMM–Newton*'s Reflection Grating Spectrometer. These measurements have been broadly corroborated by imaging spectroscopy with *Chandra* (Humphrey & Buote 2006; Athey 2007, hereafter HB06, Ath07, respectively), which, at the cost of lower spectral resolution, offers a greater effective area, wider bandwidth, better isolation of the diffuse gas, and the possibility of spatially excising contaminating flux from resolved X-ray point sources. At first sight, the presence of enriched hot gas in ellipticals supports a simple 'internal origin' for the gas, whereby its metallicity directly reflects that of the evolved stellar populations comprising the galaxy (which are approximately near solar, e.g. Trager et al. 2000a,b; Terlevich & Forbes 2002; Gallazzi et al. 2006), and appears difficult to reconcile with the notion that the hot CGM contains a large amount of metal-poor gas accreted from the IGM.

In this paper, we extend the analysis of the hot CGM of $z = 0$ GIMIC galaxies presented in Paper I, to confront the simulations with the observational constraints on coronal metallicities presently available in the literature. We demonstrate that the simulations are compatible with the data, and elucidate the nature of the enrichment of the hot CGM of $\gtrsim L_\star$ galaxies, demonstrating how, where and when the metals were injected. Building on the arguments presented in Paper I, we consider this compatibility to be further evidence that

[1] Since we are mainly concerned here with $\sim L_\star$ galaxies, we do not consider galaxies with significant AGN activity, as were considered theoretically by e.g. Ciotti & Ostriker (1997, 2007), nor those confined by the potential of galaxy groups.

[2] The first metallicity measurement of the hot CGM of a *late-type* galaxy (NGC 891) was reported by Hodges-Kluck & Bregman (2013) during the preparation of this manuscript. They report $Z \sim 0.1\,{\rm Z}_\odot$, consistent with the gas being primarily sourced by accretion from the IGM.

X-ray data support the canonical view of galaxy formation in the CDM paradigm, in a fashion that is orthogonal to, for example, the confrontation of galaxy formation models with optical/IR data (e.g. the stellar mass function or the Tully–Fisher relation). This paper is laid out as follows. In Section 2, we provide a brief overview of the GIMIC simulations and our analysis of them. We confront these analyses with X-ray data in Section 3, and demonstrate how the enrichment proceeds in Section 4. Finally, we discuss and summarize our findings in Section 5.

2 METHODS

2.1 Simulations

The GIMIC simulations are described in detail in C09, where thorough discussions of the generation of the initial conditions, the simulation algorithms and initial results may be found. Techniques for computing gas-phase X-ray luminosities and stellar optical luminosities are described in detail in Paper I. Here, we present only a brief overview and limit the description to aspects that are specifically relevant to this study, referring the reader to C09 and Paper I for additional details.

Using 'zoomed' initial conditions, GIMIC follows with full gas dynamics and, at relatively high resolution for cosmological volumes, the evolution of five roughly spherical regions of comoving radius $r \sim 20\,h^{-1}$ Mpc, drawn from the Millennium Simulation (Springel et al. 2005). The remainder of the 500^3 $(h^{-1}\,\mathrm{Mpc})^3$ Millennium Simulation volume is modelled with collisionless particles at much lower resolution, thus, correctly following the cosmic large-scale structure. In order to trace a wide range of cosmic environments, the regions were chosen such that their overdensities deviate by $(-2, -1, 0, +1, +2)\sigma$ from the cosmic mean, where σ is the rms mass fluctuation on the $20\,h^{-1}$ Mpc radial scale of the regions, at $z = 1.5$.

The GIMIC initial conditions were generated at intermediate resolution[3] ($m_{\rm gas} = 1.16 \times 10^7\,h^{-1}\,\mathrm{M}_\odot$) and high resolution ($m_{\rm gas} = 1.45 \times 10^6\,h^{-1}\,\mathrm{M}_\odot$), and ran with gravitational force softening for the high-resolution particles of $\epsilon^{\rm max}_{\rm phys} = (1.0, 0.5)\,h^{-1}$ kpc for the intermediate- and high-resolution runs, respectively. The relatively large-cosmological volume traced with gas dynamics produces a sample of over 600 relatively isolated $\sim L_\star$ galaxies, making GIMIC complementary to ultrahigh resolution simulations ($m_{\rm gas} \sim 10^4\,h^{-1}\,\mathrm{M}_\odot$) of individual galaxies.

The cosmological parameters adopted for GIMIC are the same as those assumed by the Millennium Simulation and correspond to a ΛCDM cosmogony with $\Omega_{\rm m} = 0.25$, $\Omega_\Lambda = 0.75$, $\Omega_{\rm b} = 0.045$, $\sigma_8 = 0.9$, $H_0 = 100\,h\,\mathrm{km s^{-1} Mpc^{-1}}$, $h = 0.73$ and $n_{\rm s} = 1$ (where $n_{\rm s}$ is the spectral index of the primordial power spectrum). The value of σ_8 is approximately 2σ higher than inferred from the most recent cosmic microwave background (CMB) and large-scale structure data (Komatsu et al. 2011), which will affect the abundance of $L_\star$ galaxies somewhat, but should not significantly affect their individual properties.

The initial conditions were evolved from $z = 127$ to 0 with the TreePM-smoothed particle hydrodynamics (SPH) code GADGET3, a substantial upgrade of GADGET2 (Springel 2005) that features improved load balancing (as in Springel et al. 2008) and incorporates a wide array of new baryon physics modules. Radiative cooling rates are computed on an element-by-element basis by interpolating precomputed tables, generated with CLOUDY (version 07.02; Ferland et al. 1998), that specify cooling rates as a function of density, temperature and redshift, and that account for the presence of the CMB and a spatially uniform Haardt & Madau (2001) ionizing ultraviolet (UV)/X-ray background (for further details, see Wiersma, Schaye & Smith 2009a). The ionizing background is imposed at $z = 9$ and effectively quenches star formation in small haloes (Okamoto, Gao & Theuns 2008; C09). Star formation is implemented following the prescription of Schaye & Dalla Vecchia (2008), which reproduces the observed Kennicutt–Schmidt law (Kennicutt 1998) by construction.

Feedback from SNe is implemented using the kinetic wind model of Dalla Vecchia & Schaye (2008), with an initial wind velocity $v_{\rm w} = 600$ km s^{-1} and mass-loading parameter (the ratio of mass of gas that receives an impulsive kick to the mass of stars formed) of $\beta = 4$. This scheme is energetically feasible, requiring approximately 80 per cent of the total energy available from Type II SNe for our adopted choice of initial mass function (IMF), that due to Chabrier (2003). This choice of parameters produces a good match to the peak of the cosmic star formation history (see C09; Schaye et al. 2010). The timed release of individual elements by massive stars (Type II SNe and AGB stars) and intermediate-mass stars (Type Ia SNe) is incorporated following the prescription of Wiersma et al. (2009b). A set of 11 elements (H, He, C, Ca, Fe, Mg, N, Ne, O, S and Si), representing the most important radiative coolants, are followed, enabling us to determine the element abundances of individual SPH and star particles.

The GIMIC simulations are particularly well suited to the study of $\sim L_\star$ galaxies. As shown in Paper I, the implementation of efficient (but energetically feasible) feedback from SNe largely prevents overcooling on the mass scale of $L_\star$ galaxies, and is key to the reproduction of the observed X-ray scaling relation presented in that study. Indeed, GIMIC accurately reproduces the rotation speeds and star formation efficiencies of $z = 0$ disc galaxies for $10^9 \lesssim M_\star < 10^{10.5}\,\mathrm{M}_\odot$, although galaxies with $M_\star \gtrsim 10^{11}\,\mathrm{M}_\odot$ do still suffer from some overcooling (McCarthy et al. 2012b). Moreover, Font et al. (2011) demonstrated that $L_\star$ galaxies in GIMIC exhibit satellite luminosity functions and stellar spheroid surface brightness distributions that are comparable to those of the Milky Way and M31, whilst McCarthy et al. (2012a) further demonstrated that this correspondence extends also to their global structure and kinematics.

2.2 Galaxy and halo identification

We identify bound haloes using the SUBFIND algorithm presented by Dolag et al. (2009), which extends the standard implementation (Springel et al. 2001) by including baryonic particles when identifying self-bound substructures. This procedure first finds dark matter haloes using a friends-of-friends (FoF; Davis et al. 1985) algorithm, with the standard linking length in units of the interparticle separation ($b = 0.2$) It also associates all baryonic particles with their nearest neighbour dark matter particle. The aggregated properties of baryonic particles associated with grouped dark matter particles define the baryonic properties of each FoF group. Halo substructures are then identified using a topological unbinding algorithm. This provides an unambiguous definition of a *galaxy* within the simulations, namely the set of star particles bound to individual subhaloes. The gas bound to each subhalo then forms the ISM and CGM; these phases are delineated by the density threshold for the onset of star formation, $n_{\rm H} = 0.1$ cm^{-3}. Since individual haloes may have more than one 'subhalo', they may host more than one galaxy. In analogy

[3] We reserve the term 'low resolution' for the original realization of the Millennium Simulation.

to semi-analytic models, the stars associated with the most massive subhalo of an FoF group are defined as central galaxies, whilst stars associated with substructures are satellites. When referring to the mass of haloes, we adopt spherical overdensity (Lacey & Cole 1994) masses, centred on the most bound particle within FoF groups, with radius such that the mean enclosed density is 200 times the critical density, i.e. M_{200}.

2.3 Simulated galaxy sample

As in Paper I, we draw galaxies from all five intermediate-resolution GIMIC regions, and use the high-resolution -2σ region as a benchmark for brief convergence tests, which are presented in Appendix A. We impose a number of selection criteria in order to construct a sample similar to observational samples: we select central (i.e. the most massive galaxy within an FoF halo) galaxies whose stellar mass lies in the range $10^{10} < M_\star < 10^{11.5}\,\mathrm{M}_\odot$, corresponding to a fairly broad mass range bracketing $L_\star$. We additionally require that the subhalo with which each galaxy is associated should account for at least 90 per cent of the mass of the parent FoF group, i.e. $M_{\rm sub} > 0.9 M_{\rm FoF}$. This criterion is intended to select only isolated systems by excluding those that are interacting or are members of galaxy groups or clusters. These selection criteria result in a sample of 617 galaxies at $z = 0$.

As shown in McCarthy et al. (2012b), the intermediate-resolution GIMIC simulations accurately reproduce the stellar mass–rotation speed (or 'Tully–Fisher') relation at $z = 0$ for galaxies with $10^9 \lesssim M_\star < 10^{10.5}\,\mathrm{M}_\odot$. These galaxies are consistent with the $M_\star$–M_{200} relation inferred from stacked weak lensing + satellite kinematics analyses (see Dutton et al. 2010, and references therein). McCarthy et al. (2012b) also found that the most massive galaxies in our sample ($M_\star \gtrsim 10^{11}\,\mathrm{M}_\odot$, corresponding to K-band luminosities $L_{\rm K} \gtrsim 10^{11} L_{\rm K,\odot}$) exhibit some overcooling, since our feedback scheme becomes inefficient within massive haloes (see C09). We retain these galaxies in our sample in order to connect with observations of similarly massive ellipticals, but caution that these galaxies are likely hosted by dark matter haloes that are insufficiently massive, and exhibit star formation rates at low redshift that are too high.

2.4 Computing optical and X-ray luminosities

Optical and X-ray luminosities are computed in post-processing. The former are calculated individually for star particles, considering them as simple stellar populations (SSP). Star particles are formed with the IMF due to Chabrier (2003), and their spectral energy distribution (SED) is derived by interpolation over the GALAXEV models of Bruzual & Charlot (2003). The optical luminosity of each particle is obtained by integrating the product of its SED with the appropriate filter transmission function; the overall broad-band luminosity of a galaxy is then defined as the sum of the luminosities of all star particles comprising a galaxy. Since we are primarily concerned here with K-band luminosities, we do not expect dust extinction to be an important consideration.

Gas-phase X-ray luminosities are also computed on a per particle basis, following:

$$L_{\rm X} = n_{\rm e} n_{\rm i} \Lambda V, \tag{1}$$

where $n_{\rm e}$ and $n_{\rm i}$ are the number densities of electrons and ions, respectively, Λ is the cooling function in units of $\mathrm{erg\,s^{-1}\,cm^{-2}}$ (integrated over an appropriate passband, for example 0.5–2.0 keV), and $V = m_{\rm gas}/\rho$, where $m_{\rm gas}$ is the gas particle mass and ρ the gas particle density. We compute Λ by interpolating a pre-computed table generated using the Astrophysical Plasma Emission Code (APEC, v1.3.1; see Smith et al. 2001) under the assumption that the gas is an optically thin plasma in collisional ionization equilibrium. APEC cooling rates are computed on an element-by-element basis for each particle,

$$\Lambda_j(T_j) = \frac{Z_{j,k}}{Z_{k,\rm AG89}} \sum_{k=1}^{N} \lambda_k(T_j), \tag{2}$$

where T_j is the gas temperature of the jth particle, $Z_{j,k}$ is the metal mass fraction of the element k for this particle, and $\lambda_k(T_j)$ is the cooling function for the element k. The total cooling rate is arrived at by summing over the $N = 11$ most important elements for cooling (H, He, C, Ca, Fe, Mg, N, Ne, O, S and Si), which are individually and self-consistently tracked during the simulation. APEC assumes the solar abundance ratios of Anders & Grevesse (1989, hereafter AG89), but it is straightforward to rescale the cooling rates for arbitrary abundances, which we do here on a particle-by-particle basis, normalizing by the metal mass fractions assumed by AG89 ($Z_{k,\rm AG89}$), to achieve consistency with our chemodynamics implementation. For completeness, we present the solar abundances adopted by AG89 and GIMIC in Table 1. The latter corresponds to the abundances assumed by CLOUDY (version 07.02, last described by Ferland et al. 1998). Our scheme excludes gas within the ISM (particles with non-zero star formation rate, see Schaye & Dalla Vecchia 2008) since we assign these particles a temperature of $T = 10^4$ K.

Table 1. Abundances of the 11 elements tracked self-consistently within the GIMIC simulations, and used to compute the radiative cooling rate and X-ray luminosity of gas, presented for the Anders & Grevesse (1989) abundance standard (assumed by the APEC model), and that adopted by the GIMIC simulations, which is derived from CLOUDY (version 07.02). We follow the convention $\log_{10} N_{\rm H} = 12$.

Element	AG89	CLOUDY
Hydrogen	12.00	12.00
Helium	10.99	11.00
Carbon	8.56	8.39
Calcium	6.36	6.36
Iron	7.67	7.45
Magnesium	7.58	7.54
Nitrogen	8.05	7.93
Neon	8.09	8.00
Oxygen	8.93	8.69
Sulphur	7.21	7.26
Silicon	7.55	7.54

2.5 Computing iron abundances

Since iron has the strongest diagnostic lines in the soft X-ray band, $Z_{\rm Fe}$ is the most commonly used proxy for gas-phase metallicities in low-temperature plasmas (Loewenstein & Mushotzky 1998). We therefore adopt the mass-weighted iron mass fraction as a metallicity proxy, computed thus:

$$Z_{\rm Fe}^{\rm mw} = \frac{\sum_j^N Z_{{\rm Fe},j} m_j}{\sum_j^N m_j}, \tag{3}$$

where $Z_{{\rm Fe},j}$ is the SPH kernel-weighted iron abundance of the jth gas particle (see discussion in Section 2.6) and m_j is its mass. The

sum runs over the N gas particles associated with each galaxy that have a non-zero soft X-ray luminosity (and thus comprise the hot CGM, see Section 2.4).

In Paper I, we cautioned that the sensitivity of the X-ray emissivity of gas to density, temperature and metallicity can lead to an unrepresentative view of the overall state of hot gas. In more specific terms, the unavoidable luminosity weighting of X-ray observations can yield measurements that differ markedly from an ideal, mass-weighted measurement. The most direct comparison between simulated and observed coronae is obtained by deriving $L_{\rm X}$-weighted quantities in the former. Therefore, we also define a luminosity-weighted metallicity indicator, that is appropriate when comparing with observationally inferred metallicities, by exchanging the particle masses (m_j) in equation (3) for their SPH kernel weighted soft X-ray luminosities ($L_{{\rm X},j}$):

$$Z_{\rm Fe}^{\rm lw} = \frac{\sum_j^N Z_{{\rm Fe},j} L_{{\rm X},j}}{\sum_j^N L_{{\rm X},j}}. \quad (4)$$

In general, we use the mass-weighted measure to assess the physical state of the hot CGM, and reserve the luminosity-weighted measure for direct comparisons with observationally inferred measurements.

2.6 Metal mixing

The cooling rate, and therefore star formation rate, of cosmic gas is strongly affected by its metallicity, so the mixing of stellar nucleosynthetic products into the ISM and CGM is clearly of significance for models of galaxy evolution. The process of metal mixing, however, remains poorly described by theory, and poorly constrained by observation.

Nonetheless, a common theme amongst both types of study is that mixing is not particularly efficient, across a broad range of scales. On relatively small scales (a few parsecs), the Eulerian simulations of Parriott & Bregman (2008), and particularly Bregman & Parriott (2009), indicate that much of the ejecta from evolved stars and planetary nebulae remain unmixed with the hot ISM/CGM. This picture appears to be corroborated by observations of the structure of stellar ejecta at both IR (Wareing et al. 2006) and UV (Martin et al. 2007) wavelengths. On significantly larger scales, Schaye, Carswell & Kim (2007) argue that the large population of compact, intergalactic C IV absorbers seen in their sample of quasar sightlines is evidence for inefficient mixing of metals entrained in winds and transported from the ISM into the CGM/IGM.

The physical interpretation of the distribution and transport of metals seen in our simulations therefore requires an understanding of the behaviour and limitations of the numerical implementation of these processes. The formulation of SPH naturally defines three spatial scales for which a discussion of metal mixing is appropriate: scales smaller than, comparable to, or larger than the SPH kernel (i.e. the smoothing length).

On the smallest scales, the nucleosynthetic products of stellar evolution are implicitly assumed to be completely mixed, since the metal mass released by the SSP represented by each star particle is assigned to neighbouring SPH particles. Clearly, each particle is the smallest unit over which mass can be distributed, so it is therefore possible that on subgrid scales mixing is overestimated. Such scales are, by definition, below the resolution limit of the simulation, and as such physical insight should not be drawn from the simulations on these scales.

On scales comparable to the kernel, the finite numerical sampling of the fluid, and the absence of implicit diffusion of scalar quantities associated with SPH particles, suppresses the mixing of entropy and metals[4] (Wadsley, Veeravalli & Couchman 2008). This shortcoming is clearly of relevance here, and it has been shown that the metallicity of circumgalactic gas in simulations is increased when subgrid models for efficient turbulent mixing are imposed (Shen, Wadsley & Stinson 2010). However, we opt against imposing such a scheme here, since it represents an attempt to resolve a numerical problem with a model of a poorly understood physical process.

We intend to explore small-scale diffusion in future work, using SPH schemes augmented with higher order dissipation switches (e.g. Read & Hayfield 2012) that diffuse scalar quantities implicitly. Here, we follow Wiersma et al. (2009b) and minimize the sampling problem by computing cooling rates, X-ray luminosities and overall coronal iron mass fractions (equations 3 and 4) using kernel-weighted element abundances averaged over a given SPH particle's neighbours. The resulting smoothed metallicity complements the 'particle metallicity' that is the sum of the element mass fractions carried by each particle. This process has the potential to bias the recovered metallicity of hot circumgalactic particles, because smoothed metallicities are computed using all SPH neighbour particles, irrespective of their thermal state. The smoothed element abundances of hot particles close to the disc–corona interface are therefore computed from both cold (i.e. ISM) and hot (coronal) particles. We gauge the degree to which mixing on the scale of the kernel influences our conclusions, by comparing results derived from particle and smoothed metallicities. We conclude from this analysis, presented in Appendix B, that mixing on the scale of the kernel has no bearing on our findings.

On larger scales still, simulations indicate that the distribution of metals is governed chiefly by winds driven by energetic feedback (Wiersma, Schaye & Theuns 2011), a process self-consistently modelled by our simulations. Whilst the standard implementation of SPH is well understood to suppress the development of Rayleigh–Taylor and Kelvin–Helmholtz instabilities that would assist the mixing of metals entrained in winds into their ambient medium, the inefficient mixing inferred by Schaye et al. (2007) on these relatively large scales suggests that it is reasonable to conclude that predictions of the large-scale distribution of metals derived from our simulations are robust to the implementation of metal mixing adopted by our simulations. It is the metal distribution on these large scales that is the central focus of this study.

2.7 Stacked maps

To illustrate the correspondence of the simulated galaxies with observable properties, we present in Fig. 1 maps derived from stacking the 148 galaxies from our sample whose halo masses lie in the range $10^{12.00} < M_{200}[{\rm M}_\odot] < 10^{12.25}$. The maps are 500 kpc across, with the exception of the bottom-left panel, which is zoomed-in to 50 kpc, and in each case the galaxies have been rotated into the edge-on orientation by aligning the vertical axis with the angular momentum vector of all stars within 35 kpc of the galactic centre. The left-hand column shows the soft X-ray surface brightness ($\Sigma_{0.5-2.0\,{\rm keV}}$) of the hot CGM, the central column shows the surface density of the hot CGM ($\Sigma_{\rm hotCGM}$; top) and of stars (Σ_*; bottom), whilst the right-hand column shows the iron abundance of the hot CGM ($Z_{{\rm Fe,\,hotCGM}}$; top) and of stars ($Z_{{\rm Fe},\,*}$; bottom).

[4] It is not clear that Eulerian algorithms present a more appealing alternative, since they can in fact mix gas too efficiently (e.g. Mitchell et al. 2009).

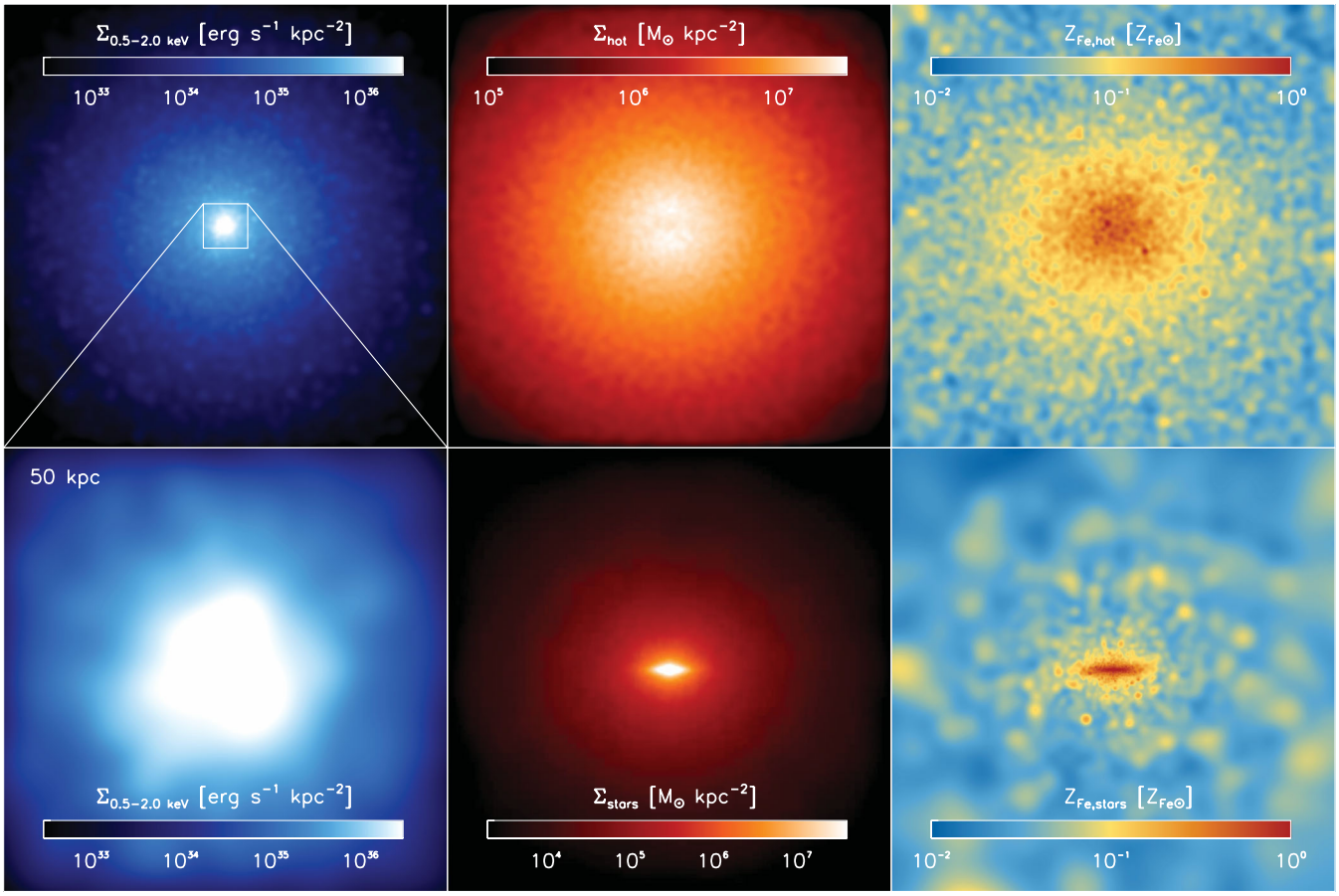

Figure 1. Stacked maps of the baryons associated with the 148 GIMIC galaxies (from our sample of 617) with halo mass in the range $10^{12.25} < M_{200}/\mathrm{M}_\odot < 10^{12.50}$. The galaxies have been rotated so that the angular momentum of stars is parallel to the vertical axis prior to stacking. The maps are 500 kpc across, with the exception of the bottom-left panel, which is zoomed to 50 kpc. Left-hand column: the soft X-ray (0.5–2.0 keV) surface brightness. Centre column: the surface density of hot gas (top) and stars (bottom). Right-hand column: the iron abundance of hot gas (top) and stars (bottom). The X-ray emission is markedly more centrally peaked than the mass distribution of the hot CGM, owing to its strong dependence on density, metallicity and temperature. A halo wide iron abundance gradient is evident in the hot CGM, that does not trace the underlying distribution of stars, indicating the prevalence of metal transport.

The alignment procedure is clearly effective: a disc can be seen in the stellar surface density map, as can the spheroidal stellar halo component that was explored by Font et al. (2011) and McCarthy et al. (2012a). Similarly, the stellar iron abundance shows a clear disc plane, and a large-scale gradient similar to the metallicity gradients observed in nearby stellar haloes (Foster et al. 2009; Spolaor et al. 2010). The presence of strong disc features in these maps is unsurprising, as roughly two-thirds of the galaxies comprising our sample are disc dominated (see Paper I). The hot gas maps exhibit circular surface density and soft X-ray surface brightness distributions, indicative of a quasi-spherical hot CGM associated with the galaxies. The coronal iron distribution is centrally peaked, but does not trace the underlying stellar iron abundance, indicating that metal transport is important for enriching the hot CGM. We return to the issue of metal transport in Section 4.

A qualitative difference in the radial distribution of the coronal gas and its X-ray luminosity is evident in the maps: the former is much more extended than the latter. This follows from the complex mapping of the state of the ionized plasmas (ρ, T, Z) into an X-ray emissivity: bremsstrahlung radiation is weakly dependent on temperature ($\propto T^{1/2}$) and strongly dependent on density ($\propto \rho^2$), whilst the metal line emission that dominates the emissivity of low-temperature plasmas is also dependent on the abundance of metals.

A quantitative assessment of the difference is presented in Fig. 2, where we bin the stacked maps radially, and plot the radial surface density of the hot CGM (black) and its X-ray surface brightness (red). The solid lines show the median value of each quantity, arbitrarily normalized to peak at a value of unity, whilst the shaded regions represent the scatter between the 10th and 90th percentiles. The inset plot presents the same data on logarithmic axes, and the overplotted dashed green lines represent fits, using the commonly adopted β-function:

$$\Sigma(r) \propto \left[1 + \left(\frac{r}{r_\mathrm{c}}\right)^2\right]^{(0.5-3\beta)} \quad (5)$$

to the stacked surface density and surface brightness profiles, where r_c is the core radius and β characterizes the profile shape. It is immediately evident that X-ray emission does not trace the hot gas mass in a simple fashion: the surface brightness profile is much more centrally peaked than the surface density profile. This is reflected quantitatively in the least-squares reduced parameters of the fitted β-functions: the surface density is best described by (r_c, $\beta = 120$ kpc, 0.59), whilst the surface brightness is best described by (r_c, $\beta = 12$ kpc, 0.56). The recovered β values are consistent with those derived from a Monte Carlo Markov chain analysis

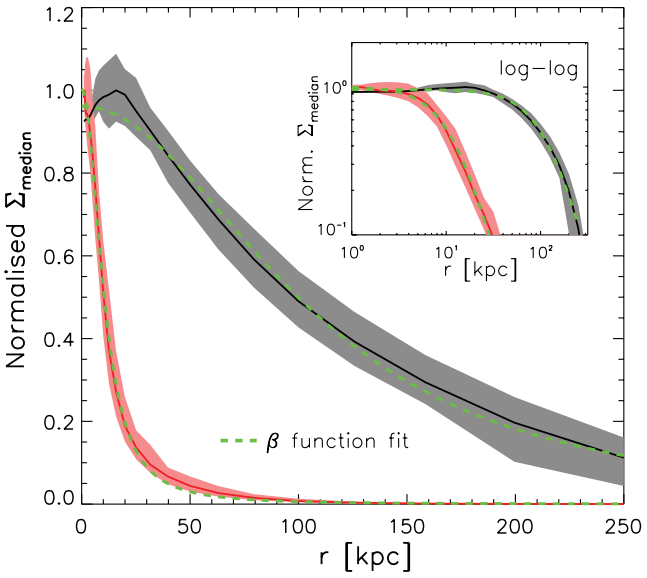

Figure 2. Circularly averaged median projected radial profiles of the surface density of the hot CGM (black) and its soft X-ray surface brightness (red), derived by radially binning the maps presented in Fig. 1, and normalizing to the maximum value of the median in each case. The shaded regions represent the scatter between 10th and 90th percentiles, and the inset plot presents the same data on logarithmic axes. The green dashed lines represent best-fitting β functions to both profiles (see the text for parameters). It is clear that the surface brightness is much more centrally peaked than the surface density, and therefore that X-ray emission does not trace the hot gas mass in a simple fashion.

of stacked *ROSAT* pointings of 2165 galaxies from the Two Micron All-Sky Survey (2MASS) Very Isolated Galaxy Catalogue, recently presented by Anderson, Bregman & Dai (2013), and similar to the values derived from deep observations of NGC 1961 and UGC 12591 by Anderson & Bregman (2011) and Dai et al. (2012), respectively. Those authors infer 1 kpc cores for NGC 1961 and UGC 12591, and constrain the stacked core radii to 0.5–5.0 kpc. This is somewhat smaller than the core radius we recover from our stacked surface brightness profile, highlighting a potential shortcoming of the simulations and an interesting avenue for future study. However, having also fitted β-functions to the individual profiles of the well-sampled galaxies in our sample, we find that a wide range of core radii is recovered; a small but significant fraction of the profiles ($\sim$15 per cent) is in fact best described by cusped profiles ($r_c \rightarrow 0$). The simulations therefore yield a non-negligible fraction of galaxies that are similar to those observed. Moreover, we caution that the small sample of observationally inferred fits may be unrepresentative of the population we explore with the simulations, since galaxies with small core radius exhibit a greater peak surface brightness at fixed luminosity, rendering them easier to detect (cf. Rasmussen et al. 2006).

Besides highlighting that it is challenging to observe hot coronae at radii significantly beyond the optical radius of the central galaxy, Fig. 2 indicates that, in the absence of spatially resolved spectroscopy (which is extremely challenging to realize for the hot CGM of galaxies with current instrumentation), the intrinsic luminosity weighting of observations biases the coronal metallicity inferred from X-ray spectroscopy towards the high surface brightness and metal rich gas close to galactic centres. The importance of this effect will be explored in the following section.

3 THE CORONAL METALLICITIES OF PRESENT-DAY GALAXIES

In this section, we present the iron mass fractions of the hot CGM associated with GIMIC galaxies at $z = 0$, and confront them with observational measurements inferred from X-ray imaging spectroscopy. We start with a brief discussion of observational studies in the literature.

3.1 Confrontation with observational data

The excellent spatial resolution of *Chandra* has revolutionized studies of metal enrichment in galaxies and galaxy groups. The so-called Fe discrepancy (Arimoto et al. 1997; Renzini 1997), namely the inference of highly subsolar iron abundances in early-type galaxies, has been shown to result from the inability of *ROSAT* and *ASCA* to resolve coronal temperature gradients (HB06), that can lead to underestimated abundances when isothermal spectral fits are adopted (e.g. Buote & Canizares 1994; Trinchieri et al. 1994; Buote & Fabian 1998). Early studies with *Chandra* (and *XMM–Newton*) focusing on individual systems indicated near-solar coronal iron mass abundances (e.g. Buote 2002; Gastaldello & Molendi 2002; Buote et al. 2003; O'Sullivan et al. 2003; Humphrey, Buote & Canizares 2004; Kim & Fabbiano 2004). Motivated to extend this discovery to a representative sample of galaxies, HB06 uniformly reduced archival *Chandra* data for 28 nearby, early-type galaxies with soft X-ray luminosities spanning the range $10^{39} \lesssim L_X[\,\mathrm{erg\ s^{-1}}] \lesssim 10^{43}$. They report that their measurements support an absence of correlation between Z_{Fe} and L_X, and confirm that in all but one case (NGC 1553), the coronal iron abundance corresponds closely with that of the stars. A similar study was presented by Ath07, who uniformly reduced *Chandra* imaging spectroscopy data (from the ACIS-S3 instrument) for 54 nearby ($d \lesssim 110$ Mpc) early-type galaxies. For the brightest 22 galaxies in this sample, Ath07 inferred iron abundances via spectral modelling adopting variable abundance ratios, and found that only a narrow spread of ratios was required for good fits. The lower signal-to-noise ratio (S/N) of the remaining 32 fainter galaxies required that their metallicities be derived subject to the assumption that their abundance ratios follow those of the brighter galaxies. In common with HB06, Ath07 report typical iron abundances that are approximately solar. We note that 22 galaxies are present in both samples.

In this study, we adopt the HB06 sample of 28 galaxies and supplement it with the 32 galaxies from Ath07 that are not present in HB06; in general these are fainter systems than were studied by HB06. For reference, we show briefly in Appendix C how closely the Z_{Fe} and L_X measurements inferred by these two studies match. Whilst we refer the reader to HB06 and Ath07 for detailed descriptions of the data reduction, it is appropriate to discuss key aspects of their analyses. First, Ath07 adopt the superceded solar abundance standard of AG89, whilst HB06 adopt the more recent standard of Asplund, Grevesse & Sauval (2005), which is very similar to that adopted by GIMIC. For consistency, in what follows, we therefore multiply the iron abundances derived by Ath07 by a factor of 1.65 to achieve consistency between the adopted standards. Where the signal-to-noise ratio of the X-ray spectroscopy allows both studies to fit plasma models with variable abundance ratios; in the event of insufficient S/N, HB06 fix to solar ratios, whilst Ath07 adopt the typical ratios of the high-S/N galaxies. HB06 report estimated 'global abundances', whereby systems with measurable abundance gradients are fit by a power law and extrapolated to 30 arcmin. Ath07 report

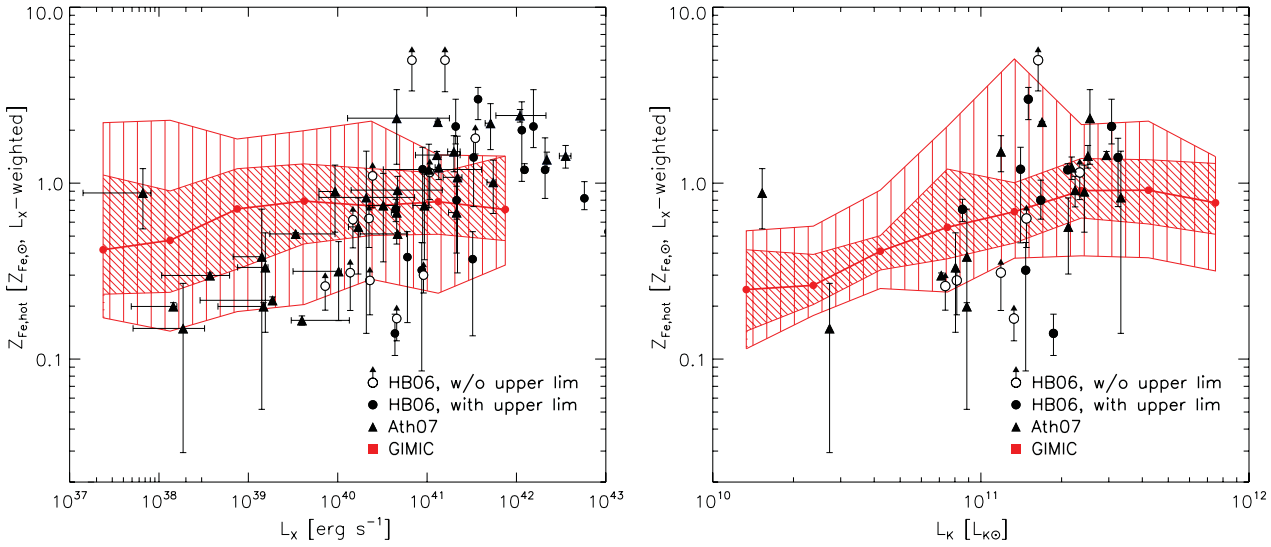

Figure 3. The X-ray luminosity-weighted iron abundance of circumgalactic gas, as a function of soft X-ray luminosity (left) and the *K*-band luminosity of galaxies (right). The left-hand panel comprises the 28 nearby elliptical galaxies analysed by HB06 (circles) and the 26 (from a total sample of 54) nearby ellipticals from the sample of Ath07 (triangles) that do not overlap with the HB06 sample. The right-hand panel comprises the subset of the overall galaxy sample for which *K*-band magnitudes are available in the 2MASS Large Galaxy Atlas. The open circles with upward arrows represent cases where the HB06 spectral analysis yielded no formal upper limit on the iron abundance. Symbols are overplotted on the median L_X-weighted Z_{Fe}–L_X and Z_{Fe}–L_K relations of galaxies in the GIMIC simulations, with 1σ and 2σ scatter shown by the densely and sparsely hatched red regions, respectively. Although the correlation between Z_{Fe} and L_X, implied by the addition of the Ath07 sample to the HB06 sample, is not reproduced by the simulation (but see Appendix C), the normalization of the observed metallicities is broadly reproduced by the simulations.

hot gas abundances within one effective (optical) radius of the host elliptical. Finally, we note that the spectral analysis performed by HB06 produced no upper bound on the iron abundance of 12 of 28 galaxies in their sample; we plot these as the open circles with no upper error bar.

We compare the Z_{Fe}–L_X relation of the HB06 and Ath07 samples with the GIMIC results in the left-hand panel of Fig. 3. The observational measurements are overplotted on the median and 1σ and 2σ scatter (represented by the densely and sparsely hatched regions, respectively) of the L_X-weighted coronal iron abundance of the 617 galaxies in the GIMIC $\sim L_\star$ galaxy sample. The GIMIC sample does not extend to such high soft X-ray luminosities ($>10^{42}$ erg s^{-1}) as the data, since overcooling in haloes with these luminosities produces galaxies that are much more massive than $L_\star$ at $z = 0$ and are hence excluded from our sample.

The simulated galaxies exhibit no strong correlation between the L_X-weighted iron abundance and L_X, with a median Z_{Fe} that is near solar across five decades in L_X, and a 2σ scatter of approximately one decade in Z_{Fe}. This absence of correlation suggests that simulations with efficient feedback in massive haloes would not generate significantly different iron abundances to those shown here. In fact, McCarthy et al. (2010) showed that including efficient feedback in galaxy groups, implemented as AGN feedback in the OWLS simulations (Schaye et al. 2010), has almost no impact upon the iron injected into the hot intragroup/intracluster medium, even though the mass of stars in galaxy groups/clusters is suppressed by a factor of 4. This is because the additional iron that is synthesized in simulations without AGN feedback is mostly injected into the cold ISM (rather than the hot CGM), and is rapidly reincorporated into subsequent generations of stars.

HB06 concluded that their sample shows no convincing evidence of a correlation between Z_{Fe} and L_X. The addition of the Ath07 data, which populate the Z_{Fe}–L_X plane at lower luminosities, indicate an increase in metallicity from low- to high-luminosity systems. The simulated sample does not exhibit such a pronounced correlation. Whilst this potentially represents a shortcoming of the simulations, we note that the correlation remains ill understood observationally and, as discussed by Buote & Fabian (1998) and HB06, the recovery of Z_{Fe} is potentially hampered by complex, multicomponent thermal structure in the hot gas. This tends to bias the measurement towards low abundances. A second potential shortcoming of the model is the absence of galaxies with $Z_{Fe} \gtrsim 2\,Z_\odot$, as are present in the HB06 sample. We again caution, however, that the quoted uncertainties potentially underestimate the true uncertainty of each measurement. As an example, we note that NGC 4365 features in both samples: HB06 infer a metallicity of $Z_{Fe} = 5\,Z_\odot$, whilst Ath07 assigns it a subsolar metallicity. This uncertainty is discussed further in Appendix C.

We stress that it is not our aim to advance the GIMIC simulations as a complete and detailed description of the CGM as observed in soft X-rays. Whilst a detailed dissection of the establishment of the Z_{Fe}–L_X relation is clearly an interesting avenue for future study, it is our aim here to test whether observational measurements rule out the general framework within which the hot CGM is established primarily via the accretion and heating of metal-poor intergalactic gas, as proposed in Paper I. The left-hand panel of Fig. 3 demonstrates conclusively that the presence of a hot CGM, dominated by low-metallicity gas accreted from the IGM, is perfectly consistent with luminosity-weighted, near-solar metallicities. In our cosmological simulations, in which most of the hot CGM is of extragalactic origin, the median luminosity-weighted iron abundance of the gas is typically $\sim$0.4–0.7 $Z_\odot$, with 2σ scatter between $\sim$0.2 and 1.1 $Z_\odot$, across five decades in X-ray luminosity. Thus, our simulations demonstrate that the often used argument that high metallicities preclude a predominantly extragalactic origin for the hot CGM of typical galaxies is not robust.

As a consistency check we plot, in the right-hand panel of Fig. 3, the Z_{Fe}–L_K relation for the subset of galaxies in the HB06 and Ath07

samples for which *K*-band magnitudes are available in the 2MASS Large Galaxy Atlas (Jarrett et al. 2003).[5] The data exhibit a larger scatter (approximately two decades in $Z_{\rm Fe}$ at $L_{\rm K} = 10^{11}\,{\rm L_{K,\odot}}$), which is broadly consistent with the simulations. The simulations indicate a weak correlation that is broadly consistent with the observational measurements over this luminosity range. The $L_{\rm X}$–$L_{\rm K}$ relation for GIMIC galaxies was presented in Paper I, where it was shown to accurately reproduce the observed relation for disc galaxies. We intend to present a comparison with both disc and elliptical galaxies in a forthcoming paper (Crain et al. in preparation).

There is a reasonable match between the results of the simulated galaxies and the observational measurements: nearly all of the measurements lie within the 2σ scatter of the simulation results, over five decades in $L_{\rm X}$. This is remarkable given that the parameters of the subgrid modules in the simulations were not tuned to reproduce any particular X-ray scaling relations. We conclude that models of galaxy formation based upon the CDM paradigm in which the hot CGM of $\gtrsim L_\star$ galaxies is dominated by gas accreted from the IGM are consistent with the best available observational constraints on the heavy element abundance of hot gas associated with such galaxies.

3.2 Recycled mass and luminosity profiles

As motivated in Section 1, the correspondence of near-solar coronal iron abundances measured in the data and in the simulations may at first seem surprising, since it was shown in Paper I (see fig. 12 of that study) that the hot CGM of the simulated galaxies is dominated by metal-poor gas accreted from the IGM. To understand how these findings are reconciled, we probe the enrichment of the simulated coronae in greater detail in this section.

We remarked earlier, upon inspection of the surface density and surface brightness profiles presented in Fig. 2, that luminosity-weighted X-ray measurements provide an unrepresentative view of the state of hot CGM, because the X-ray emission does not trace the hot gas mass in a simple fashion. The effect of this bias on the inferred metallicity of the hot CGM is highlighted in Fig. 4, where we plot the mass-weighted equivalent of Fig. 3 for the simulated galaxy sample. Each galaxy is represented by a filled circle whose colour encodes its halo mass, M_{200}, and a clear correlation between $L_{\rm X}$ and halo mass is evident (see also fig. 6 of Paper I). Low-luminosity galaxies exhibit a slightly greater median iron abundance and a larger scatter than their higher luminosity counterparts, because the hot CGM associated with these systems is comprised of a greater fraction of gas recycled from evolved stars than is the case for more massive galaxies, as we discuss below. However, the median value of $Z_{\rm Fe}$ is typically $\lesssim$0.1 $\rm Z_\odot$ across the range of luminosities probed here. This contrasts with the $L_{\rm X}$-weighted measurement, which is near solar across five decades in $L_{\rm X}$. The colour coding reveals the strong correlation between $L_{\rm X}$ and halo mass (see also fig. 6 of Paper I). For comparison, the inset panel shows the luminosity-weighed measurements from which the median and scatter shown in Fig. 3 were obtained.

The hot CGM of a typical $\sim L_\star$ galaxy in our simulation sample at $z = 0$ is therefore metal poor, indicating that the hot gas is not comprised primarily of the products of stellar evolution. It is possible to check this explicitly, since the gas mass 'recycled' by the stellar populations represented by star particles is shared amongst their neighbouring SPH particles. Any difference between an SPH particle's mass at $z = 0$ and the start of the simulation is therefore solely due to enrichment by stellar evolution. In Fig. 5, we separate the simulated sample by halo mass into bins of $\Delta\log_{10}M_{200}[\,{\rm M_\odot}] = 0.25$. The left-hand panel shows the spherically averaged radial profile of the median recycled mass fraction of particles comprising the hot CGM and, for reference, we plot in the inset the equivalent profiles for the entire CGM, irrespective of its thermal state. There is a strong radial dependence, such that the products of stellar evolution are, unsurprisingly, found close to the stars themselves, near the halo centre (metals are, nonetheless, transported to large radius, as we discuss in Section 4.3). The overall fraction of the hot CGM contributed by recycling is greatest for the lowest mass systems, as can also be seen in Fig. 4, for two reasons. First, the characteristic virial temperature of these systems is low, so a smaller fraction of their accreted gas is X-ray luminous (and hence becomes part of the 'hot CGM'). Secondly, the baryon fraction of low-mass haloes is lower than that of haloes hosting brighter galaxies because gas is more efficiently ejected by winds in the former.[6] The metal mass injected into the hot CGM by stellar evolution is therefore diluted by a smaller mass of metal-poor gas accreted directly from the IGM.

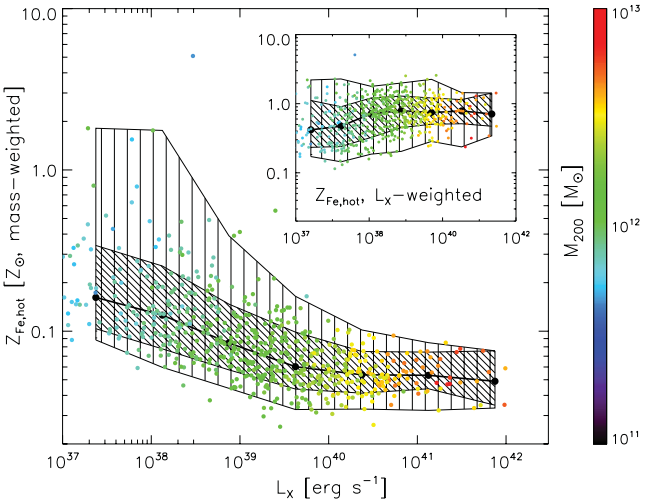

Figure 4. The mass-weighted $Z_{\rm Fe}$–$L_{\rm X}$ relation of GIMIC galaxies. Galaxies are represented by the circles whose colour encodes the galaxy's halo mass, whilst the solid line, densely hatched and sparsely hatched regions show the median (hot gas) mass-weighted $Z_{\rm Fe}$, and its 1σ and 2σ scatter, respectively. For reference, luminosity-weighted measurements (as in the left-hand panel of Fig. 3) are plotted in the inset. Although the $L_{\rm X}$-weighted iron abundances are consistent with the near-solar values inferred from X-ray data, the hot CGM is metal-poor in a mass-weighted sense. Moreover, X-ray luminosity can be seen to correlate strongly with halo mass. These findings are expected if the hot CGM is established primarily via the accretion of gas from the IGM.

[5] Whilst all of the galaxies of the HB06 and Ath07 samples are included in the 2MASS Extended Source Catalogue, the integrated fluxes of these nearby galaxies are recorded inaccurately, because of their proximity to scan edges. The 2MASS Large Galaxy Atlas accounts for this inaccuracy by combining adjoining scans.

[6] The baryon fraction of GIMIC galaxies is a strong function of halo potential. At $z = 0$, the typical baryon fraction increases smoothly from 10 to 90 per cent of the cosmic fraction for galaxies with circular velocities between $100 \lesssim v_{\rm c} \lesssim 400$ km s^{-1} (see fig. 12 of C09), and exhibits significant scatter. This value is particularly sensitive to the details of the adopted feedback prescription (e.g. Haas et al. 2012), and it is likely that the baryon fraction of massive galaxies here is overestimated owing to the omission of efficient feedback in massive haloes, such as that from AGN.

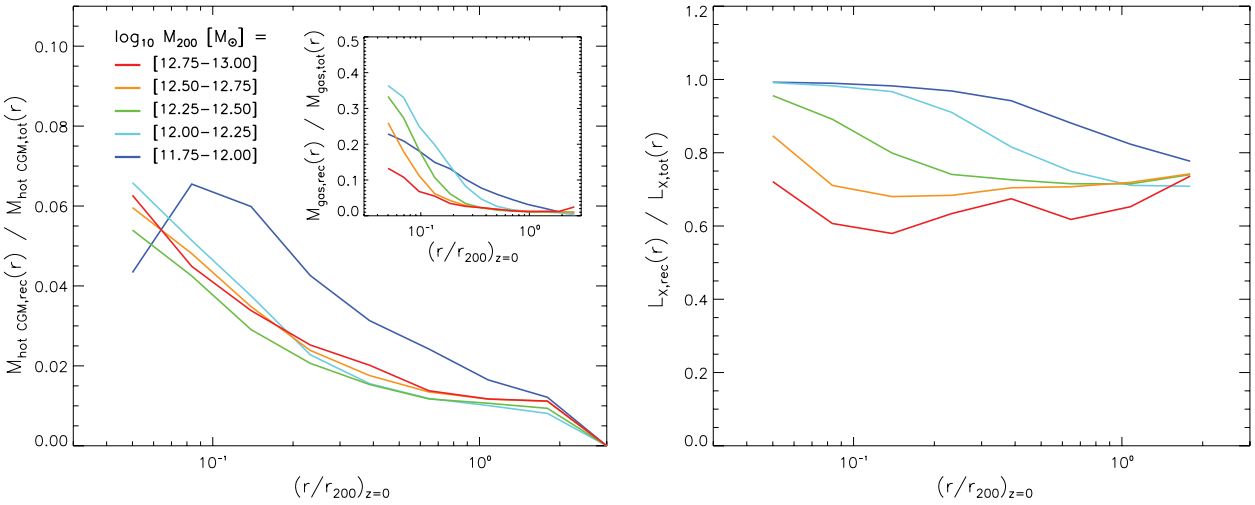

Figure 5. Left: spherically averaged radial profiles of the fraction, by mass, of the hot CGM contributed by gas recycled by stellar evolution. Galaxies have been binned by M_{200} (see legend). The inset shows the contribution to all halo gas (ISM + CGM), irrespective of thermal phase (note the different y-axis ranges). The contribution of recycled gas to the hot CGM is less than 10 per cent at all radii (though the contribution to the ISM and cold CGM phases can be several times this). The small fraction of hot recycled gas is largely confined to small radii, close to the stars that produce it. Right: as left, but showing the fraction of soft X-ray luminosity produced by recycled gas. In spite of recycled gas contributing a small fraction of the hot CGM mass, it dominates the diffuse soft X-ray emission of the galaxy at all radii. This leads to the marked difference between the mass-weighted and luminosity-weighted metallicity seen in Fig. 4. Note the markedly different scales on the y-axes of the three plots.

The overall contribution of recycled gas to the hot CGM is, nonetheless, small at all radii for haloes of any mass: even near the halo centre, recycled gas comprises less than 10 per cent of the hot CGM (as also shown in Paper I), and integrated over the entire hot CGM the contribution is typically only a few per cent. By contrast, as shown by the inset plot, recycled gas contributes a significant (but not dominant) fraction when considering all gas bound to the halo (i.e. ISM + all CGM gas, irrespective of thermal phase). Therefore, a significant fraction of metals synthesized by the stars comprising today's L_* galaxies have either been ejected into the IGM (see also Ciotti et al. 1991), or recycled into a cool phase (i.e. the ISM or cold CGM) from which they can become locked up in subsequent generations of stars (e.g. Leitner & Kravtsov 2011).

In the right-hand panel of Fig. 5 we show the fraction of the diffuse soft X-ray luminosity produced by recycled gas. We compute the contribution from recycled gas on a per particle basis, by equating the ratio $L_{\rm X,\,rec}/L_{\rm X,\,tot}$ to that of the specific soft X-ray emissivities, $\Lambda_{\rm rec}/\Lambda_{\rm tot} = 1 - \Lambda_{\rm pri}/\Lambda_{\rm tot}$, where $\Lambda_{\rm pri}$ is the specific emissivity of the gas packet assuming it has primordial element abundances. As discussed by Wiersma et al. (2009b), this approach is accurate as long as the contribution of heavy elements to the free electron density is a small fraction of the total.[7] The emissivities are computed as per equation (2), summing over 11 elements for each particle, albeit with the element abundances (Z_k in equation 2) of elements heavier than helium fixed at zero in the case of $\Lambda_{\rm pri}$.

In contrast to the mass fraction shown in the left-hand panel, the luminosity fraction due to recycled gas dominates at all radii. This is because the specific emissivity of a ∼0.1 keV plasma is extremely sensitive to the presence of metal ions. The effect is most dramatic in the case of low-mass galaxies, which retain a smaller fraction of their baryons in the form of an accreted, quasi-hydrostatic corona (see C09), and in which galactic winds are more efficient at transporting enriched gas from the galaxy into the CGM and IGM in the GIMIC simulations. In addition, the bias between the recycled mass and luminosity fractions is expected to be largest for low-mass galaxies, because the offset between the halo virial temperature and the temperature at which the emissivity of collisionally excited iron peaks is greatest for these systems (van de Voort & Schaye 2013). Nonetheless, the emissivity of the hot CGM associated with even the most massive galaxies in our sample is dominated by recycled gas. Since the hot CGM of typical galaxies remains extremely challenging to detect in emission, we infer from our simulations that the presence of metals in the hot CGM is a crucial aspect of its 'observability', since they exhibit a far higher specific emissivity than hydrogen and helium ions.

It is important to clarify at this juncture what is meant by 'recycled gas'. In the context of Fig. 5, it would be more accurate to use the term 'recycled ions': the mass of the plasma is dominated by ions (as opposed to electrons), and when computing the plasma luminosity, we sum over individual ionic species. Physically, however, the line emission is the result of collisions between ions and electrons (or, in the case of the Bremsstrahlung radiation that dominates more energetic plasmas, the result of the deflection of electrons by ions). Whilst the metal ions that dominate the emissivity of the plasma result from internal, stellar evolution processes; the left-hand panel of Fig. 5 indicates that the mass density, and therefore the electron density, of the hot CGM is dominated by the metal-poor plasma accreted from the IGM. We therefore conclude that the observability (in emission) of the hot CGM of typical galaxies requires both the outward transport of heavy elements from the central galaxy and the accretion of gas from the IGM to compress and heat the recycled gas, and to provide electrons that can excite the metal ions.

3.3 Iron abundance mass profiles

The declining contribution of gas recycled by stellar evolution to the mass of hot CGM at large radii is reflected in the radial profile of its

[7] For gas of solar composition, approximately 1 per cent of electrons are contributed by metal ions.

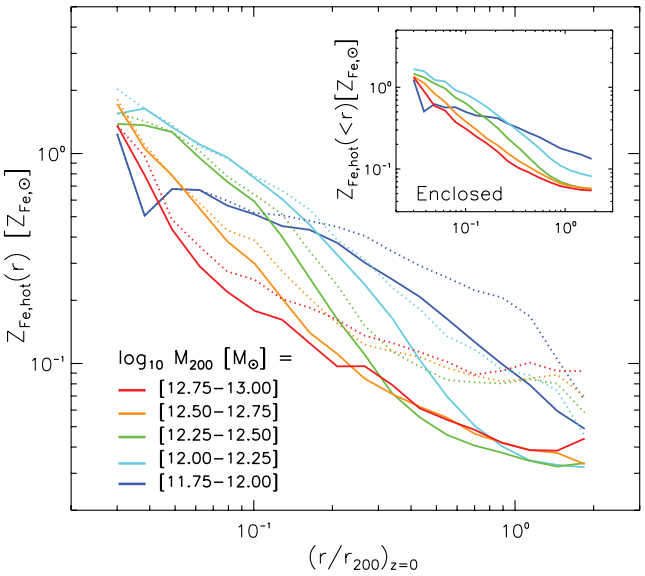

Figure 6. Spherically averaged radial profile of the mass-weighted (solid lines) and L_X-weighted (dotted lines) iron mass fraction of the hot CGM of GIMIC galaxies, binned by M_{200} as in Fig. 5. The profiles of haloes of all masses exhibit a negative gradient. Mildly supersolar abundances are exhibited at the halo centre; the mass-weighted profiles drop to a few per cent of solar at the virial radius, whilst the L_X-weighted profiles tend to a tenth of solar, highlighting the presence of a bias in the metallicity measure at large radii. The inset panel shows mean mass-weighted iron mass fraction obtained by integrating over all hot CGM gas within a radius r. See the text for a discussion of these biases.

mass-weighted (equation 3) iron abundance, Z_{Fe}, plotted with solid lines in Fig. 6. The strong abundance gradients reflect the centrally concentrated Z_{Fe} distribution visible in the top-right panel of Fig. 1. The central iron abundance is typically supersolar, but drops to a few per cent of $Z_{Fe,\odot}$ at the virial radius (r_{200}). Such a strong metallicity gradient makes estimates of the hot CGM metallicity dependent on the radius within which it is measured. To illustrate this, we show in the inset plot the mass-weighted iron abundance recovered when integrating over the gas enclosed within a given radius, $Z_{Fe}(< r)$. Within $0.1\,r_{200}$ (approximately r_e for $L_\star$ galaxies), the typical mass-weighted iron abundance is mildly subsolar, but drops to $\sim 0.1\,Z_\odot$ if all hot CGM gas within r_{200} is considered.

Our discussion so far has focused on the fact that X-ray measurements of iron abundance are higher than the 'true' mass-weighted measurement because the strongly centrally peaked surface brightness profile of the hot CGM strongly biases the measurement towards the bright, metal-rich centre of the X-ray corona. However, we might reasonably also expect a bias between mass- and L_X-weighted iron abundance measurements *at fixed radius*, because of (i) the sensitivity of the plasma emissivity to the presence of metal ions and (ii) the tendency of metals to clump (see e.g. Nagai & Lau 2011; Simionescu et al. 2011; van de Voort & Schaye 2013), either because they induce efficient cooling and/or because they are associated with dense substructures. Clumping is indeed apparent in the stacked map of hot CGM iron abundance in Fig. 1. To assess the scale of this bias, we plot the L_X-weighted radial profile of Z_{Fe} in Fig. 6 with dotted lines. At small radii ($r \lesssim 0.2 r_{200}$), the mass- and L_X-weighted measurements are similar, but at larger radii the mass-weighted iron abundance exhibits a steeper gradient than the L_X-weighted measurement, such that at r_{200}, the latter is a factor of $\sim$3 greater than the former. We then conclude that the effect is significant, but insufficient to explain the overall offset between mass-weighted and L_X-weighted measurements of Z_{Fe} when integrated over the entire hot CGM. The combination of a centrally peaked X-ray surface brightness profile and a strong negative gradient in radial metallicity in the hot CGM is stronger than the bias at fixed radius.

In summary, it is clear that the 'true' (i.e. mass-weighted) iron abundance of the hot CGM is significantly lower than the value recovered from an L_X-weighted measurement. The marked difference between the mass-weighted and L_X-weighted iron abundances reconciles the inference of near-solar iron abundances from X-ray spectroscopy of $\sim L_\star$ galaxies with models of galaxy formation in which the hot CGM is predominantly accreted from the IGM. The unavoidable L_X-weighting of X-ray data biases the measurements towards the hot, dense and metal-rich gas (with the highest surface brightness) lying close to the galaxy. A mild bias between mass- and L_X-weighted measures exists at fixed radius because of the sensitivity of specific X-ray emissivity to the presence of metal ions. By mass, most hot CGM gas resides at large radius, where there is a greater mass of metal-poor gas, accreted from the IGM, to dilute transported metals. The rapid decline of the X-ray surface brightness of the hot CGM with galactocentric radius seen in Fig. 1 highlights why radial metallicity profiles are so challenging to determine from X-ray emission line spectroscopy. We speculate that the best prospect for constraining mass-weighted abundance profiles with existing X-ray instrumentation is to use stacked emission maps or absorption spectroscopy (e.g. Fang et al. 2010) and to compare these to synthetic observations created with hydrodynamical simulations.

4 DISSECTING THE ENRICHMENT OF GALACTIC CORONAE

Having established in Section 3 that the iron abundance of the hot CGM associated with $\gtrsim L_\star$ galaxies in the GIMIC simulations is compatible with observational constraints, we turn to a detailed analysis of how the enrichment proceeds over cosmic time. We start by examining the location of enriched gas particles at the epoch of enrichment, and ask whether they were bound to the same central galaxy they are bound to at $z = 0$, a satellite galaxy of the central galaxy, another galaxy altogether, or bound to no galaxy at all (i.e. the IGM). We also explore the radial migration of hot, enriched gas throughout the assembly history of the galaxies. We subsequently investigate whether the enrichment of the hot CGM was dominated by prompt Type II SNe detonations or by the slow release of metals (on 10^9 yr time-scales) by Type Ia SNe, AGB stars, etc.

4.1 Is the hot CGM enriched internally or externally?

To assess the relative significance of the reservoirs that contribute metals to the hot CGM of $L_\star$ galaxies at $z = 0$, we adopt a similar methodology to Font et al. (2011), who explored the contribution of various processes to the formation and assembly of stellar haloes. For each galaxy in our GIMIC sample, we separate the enrichment history of its coronal gas into four categories as follows.

(i) *In situ*: an enrichment event is flagged as 'in situ' if, at the time of enrichment, the recipient gas particle was bound to the most massive subhalo of the most massive progenitor (MMP) FoF group of the galaxy at $z = 0$.

(ii) *Satellite of MMP*: the event is flagged as 'satellite enrichment' if, at the time of enrichment, the recipient gas particle was bound to any other subhalo of the MMP.

(iii) *External galaxy*: the event is flagged as 'external enrichment' if, at the time of enrichment, the recipient gas particle was bound to any subhalo of any FoF group other than the MMP.

(iv) *Smooth*: the event is flagged as 'smooth' if, at the time of enrichment, the recipient gas particle was not part of any FoF group.

The categories are unambiguous insofar that they account for all enrichment events and are mutually exclusive.

The procedure by which we identify the MMP and classify enrichment events is as follows. For a given central galaxy at $z = 0$, we select all dark matter particles within r_{200} belonging to the dominant (most massive) subhalo. We use the unique IDs assigned to these particles to identify the FoF group in previous snapshots that contains the greatest number of these particles. This FoF group is said to be the MMP and the most massive subhalo of that FoF group is assumed to be the MMP of the dominant subhalo of the system at $z = 0$. Each of the gas particles that make up the hot CGM at $z = 0$ is tracked back in time through all previous simulation outputs ('snapshots'), and the iron mass added to the particle is assigned to one of the four categories above, based on which, if any, FoF group and subhalo the gas particle belonged to at that time.

Each GIMIC volume has approximately 60 snapshots, spanning the redshift range $z = 20$ to 0. The time of each enrichment event will not, in general, correspond to the redshift for which the snapshot data were written. We therefore must use the snapshot that is closest in time to identify where the gas particle was enriched. This could, in certain circumstances, lead to a misidentification of the location of the enrichment (i.e. to which, if any, subhalo it belonged when it was enriched). However, we have explicitly checked that this is not an important issue by rerunning our tracing algorithm using only every second snapshot, and find that the in situ enrichment fraction recovered in this case does not differ significantly; we therefore conclude that the redshift sampling of our snapshot data is sufficient to deduce whether a given particle was enriched 'internally' (i.e. in situ) or 'externally' (i.e. in a satellite, an external galaxy, or the IGM). We trace each of the $z = 0$ coronal gas particles back in time as far as $z = 10$ to determine their enrichment category. We ignore the very small fraction of metal mass synthesized at $z > 10$.

In Fig. 7, we plot the fractional contribution of these categories to the overall iron mass fraction radial profile, for the ∼350 galaxies with halo mass in the range $10^{12.00} < M_{200}/\mathrm{M}_\odot < 10^{12.50}$. Within the virial radius in situ enrichment dominates, indicating that the majority of coronal metals are synthesized by, and transported from, stars comprising the central galaxy. At large radii ($\sim r_{200}$), the 'external galaxy' category becomes significant (but not dominant), indicating that coronal outskirts are, in part, enriched by the transfer of gas from external galaxies to the MMP, for example via ram pressure stripping or entrainment within supernova-driven (SN-driven) outflows. It is clear that the contribution of external galaxies to the metal mass of hot gas confined by the potential of haloes will be a function of halo mass, since the central galaxy of galaxy groups and clusters hosts a decreasing fraction of the overall stellar mass in more massive haloes (Lin & Mohr 2004). However, even in haloes as massive as $\sim 10^{14}\,\mathrm{M}_\odot$ the central galaxy typically comprises over 50 per cent of galactic stellar mass bound to the halo, so the curves presented in Fig. 7 are unlikely to be particularly sensitive to M_{200}.

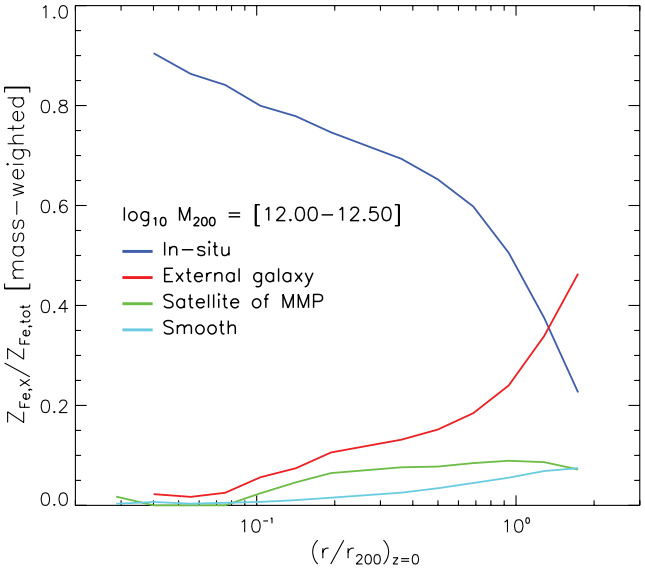

Figure 7. Spherically averaged mass-weighted radial profiles of the coronal iron mass fraction contributed by the categories of enrichment described in Section 4.1: in situ (blue), within an external galaxy (red), within a satellite of the central galaxy (green) and external to any FoF halo ('smooth', cyan). Within r_{200}, in situ enrichment dominates, indicating that the majority of coronal metals are transported from the stars comprising the central galaxy. At large radii, where relatively few in situ metals reside, metals acquired from external galaxies (e.g. by winds or ram pressure stripping) become significant, but not dominant. Satellites of the main progenitor of the galaxy contribute only a small fraction of the total metal content of the hot CGM.

The enrichment of gas associated with satellites of the MMP contributes, on average, only a small fraction of the total iron mass of the simulated coronae. This is, in part, due to our sample selection criterion that the main subhalo of an FoF group should account for at least 90 per cent of the virial mass, a criterion we imposed to ensure that we study the hot coronal gas associated with galaxies rather than major mergers or galaxy groups. However, we have confirmed that this bias is small by relaxing this criterion to require that $M_{\mathrm{sub}} > 0.5 M_{\mathrm{FoF}}$, which produces very similar results.

The contribution to the overall fraction of coronal iron from intergalactic gas ('smooth') can be viewed as an uncertainty estimate on the plotted fractions. Since GIMIC assigns the metals synthesized by star particles to their neighbouring gas particles (i.e. those within an SPH smoothing kernel), in the limit of infinite resolution nearly all gas particles should be enriched as part of an FoF ($b = 0.2$) group (the fraction of truly intergalactic stars is very small). However, the finite particle resolution of the simulation means that it is possible for the smoothing kernel of star particles to enclose a small fraction of unbound particles. Fortunately, this issue is most problematic in ill-resolved, low-mass galaxies, which synthesize only a small fraction of the cosmic heavy elements, as confirmed by Fig. 7. We therefore neglect this component in subsequent plots. We note that our findings are qualitatively consistent with those of Shen et al. (2012), who simulated the formation of a massive galaxy to $z = 3$ and found that the central galaxy was the dominant source of circumgalactic metals, with only ∼10 per cent contributed by satellite companions at that epoch.

In addition to ascertaining the mode by which gas is enriched, we can obtain a simple quantitative diagnostic that elucidates *where*

coronal gas was enriched by defining a quantity for each gas particle that we term the 'iron enrichment weighted radius', $r_{\rm Fe}$:

$$r_{\rm Fe} = \frac{\sum_i \Delta m_{i,{\rm Fe}} r_i}{\sum_i \Delta m_{i,{\rm Fe}}}, \quad (6)$$

where i sums over all enrichment events, $\Delta m_{i,\,{\rm Fe}}$ is the growth in iron mass of the gas particle per event, and r_i is the radial distance (in physical coordinates) of the enriched gas particle from the halo centre at the time of enrichment (see also Wiersma et al. 2010; Shen et al. 2012). This quantity is not followed explicitly on a timestep-by-timestep basis in GIMIC, hence we compute it in post-processing from snapshots.

In Fig. 8, we plot $r_{\rm Fe}$ as a function of $z = 0$ radius, binned by the enrichment categories defined above. Iron synthesized within external galaxies (red) was, by definition, synthesized beyond the virial radius of the MMP, but later became bound to the potential of the central galaxy halo system. This can occur as a result of metal transport due to winds driven by the external galaxy (e.g. Shen et al. 2012), or, if the external galaxy subsequently merges with the MMP, due to ram pressure stripping of the external galaxy's CGM as it interacts with the hot CGM of the MMP (Abadi, Moore & Bower 1999; Bahé et al. 2012). Externally synthesized iron exhibits a mild correlation between the $r_{\rm Fe}$ and $r(z = 0)$, such that the iron synthesized closer to the coronal centre resides closer to the galactic centre at $z = 0$.

The dominant in situ (blue) mode of iron synthesis exhibits a significant correlation between $r_{\rm Fe}$ and $r(z = 0)$. Interestingly, this curve crosses the dotted line in Fig. 8 that marks the locus $r_{\rm Fe} = r(z = 0)$, and hence the in situ iron is characterized by both inward and outward transport. The inward transport is confined to iron synthesized within ∼0.1 of the present-day virial radius of galaxies, which roughly corresponds to the scalelength of star-forming galaxy discs: this iron was likely therefore synthesized in the outskirts of galaxy discs and subsequently migrated radially in the disc plane. However, most in situ iron is transported away from the central galaxy during its assembly history. We therefore conclude that whilst both internal and external processes contribute to the enrichment of the hot CGM associated with $L_\star$ galaxies at $z = 0$, it is the internal, in situ category that dominates.

4.2 When were coronae enriched?

In analogy with the iron mass-weighted radius defined in equation (6), we can obtain a simple quantitative diagnostic that elucidates *when* coronal gas was enriched by defining an 'iron mass-weighted redshift', $z_{\rm Fe}$, for each particle (see also Wiersma et al. 2010):

$$z_{\rm Fe} = \frac{\sum_i \Delta m_{i,{\rm Fe}} z_i}{\sum_i \Delta m_{i,{\rm Fe}}}, \quad (7)$$

where, i once again represents an enrichment event, $\Delta m_{i,\,{\rm Fe}}$ is the growth in iron mass of the gas particle per event, and z_i is the epoch of enrichment. As for $r_{\rm Fe}$, we compute this quantity in post-processing and, in analogy with Fig. 8, plot $z_{\rm Fe}$ as a function of $z = 0$ radius, binned by the enrichment categories defined in Section 4.1, in Fig. 9. The enrichment categories also exhibit significant differences in this diagnostic.

Iron contributed by external galaxies was synthesized at early times (typically $1 \lesssim z \lesssim 3$), and a mild correlation between $r(z = 0)$ and $z_{\rm Fe}$ is apparent, such that the externally synthesized iron close to the coronal centre at $z = 0$ was synthesized more recently than that in the coronal outskirts. The in situ iron exhibits a strong correlation between $r(z = 0)$ and $z_{\rm Fe}$, such that the most recently synthesized iron is closest to halo centre. In situ iron found within $0.1 r_{200}$ was typically synthesized within the last 3 to 4 Gyr,

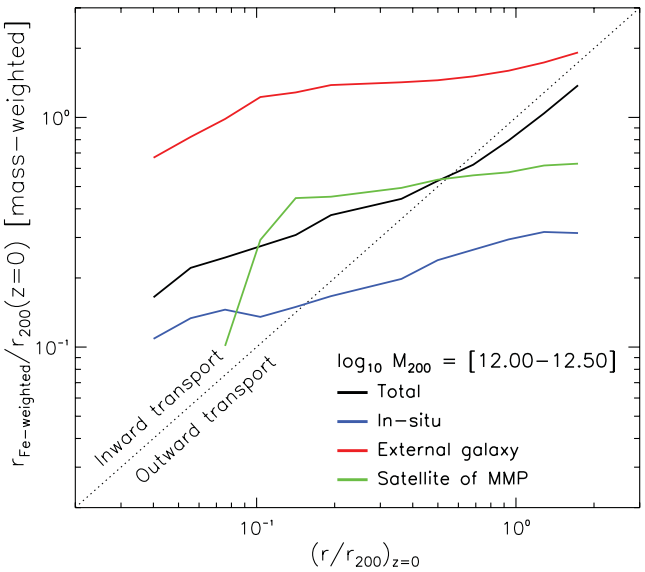

Figure 8. Spherically averaged mass-weighted radial profile of the iron enrichment weighted radius (equation 6) of coronal gas at $z = 0$, split by the enrichment categories described in Section 4.1. The diagonal dotted line marks the locus $r_{\rm Fe} = r(z = 0)$, denoting no radial migration. The mode of iron synthesis correlates strongly with the galactocentric radius at which it was synthesized, and both inwards and outwards metal transport are significant. Overall, outward transport dominates, since most coronal iron is produced in situ and redistributed by galaxy-scale winds and convection.

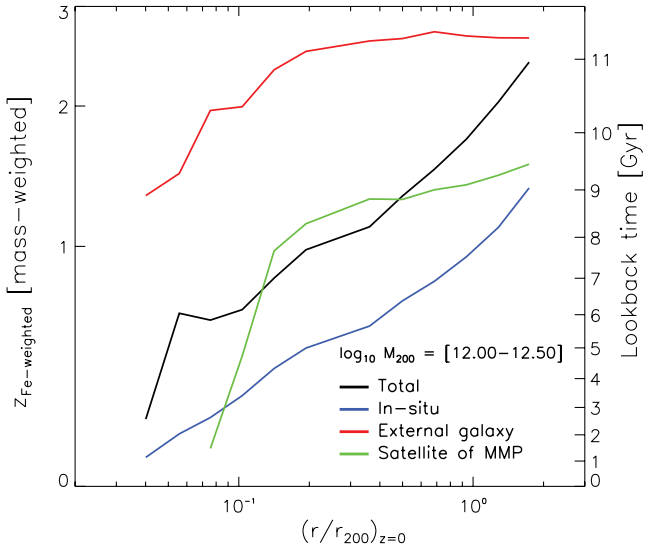

Figure 9. Spherically averaged mass-weighted radial profile of the iron enrichment weighted redshift (equation 7) of coronal gas at $z = 0$, split by the enrichment categories described in Section 4.1. The enrichment categories differ markedly, with enrichment by external galaxies occurring at relatively early times and in situ enrichment being dominant at late epochs. All categories exhibit a trend such that the metals located farthest from the galactic centre were enriched at the earliest epochs. We interpret this as a signature of a travel time, such that the metals synthesized earliest have been in transit from the galactic centre for the longest time.

whilst the in situ iron at $\sim r_{200}$ was synthesized 7 to 8 Gyr ago. This trend is a clear signature of the operation of metal transport, insofar that the iron synthesized at the earliest epochs has had the longest period of time to be transported to large radii. Interestingly, qualitatively similar trends operate for the satellite and external galaxy categories, indicating that the majority of metals synthesized in satellite and external galaxies are likely deposited close to the halo centre, and transported outwards in the same fashion as the in situ iron. This result is in qualitative agreement with Wiersma et al. (2010), who found that metals residing in low-density gas were typically ejected at early times, by low-mass haloes.

4.3 How are the metals transported?

Having established that the majority of metals in the hot CGM of today's $L_\star$ galaxies were synthesized at the halo centre and transported outwards during the assembly history of the galaxy, it is interesting to consider briefly how the transport proceeds. The entrainment of metals in galaxy winds is a natural mechanism to consider, since the winds originate at the galactic centre and propagate into the CGM. Moreover, metals entrained in outflows are readily observed at both high and low redshift (e.g. Heckman, Armus & Miley 1990; Pettini et al. 2001; Veilleux et al. 2005). The importance of metal transport by winds as a means to enrich circum- and intergalactic gas was recently studied in detail by Wiersma et al. (2011), who used cosmological hydrodynamical simulations to show that winds are the primary mechanism by which the cold–warm IGM is enriched.

However, we demonstrated in Paper I that the hot CGM of $L_\star$ galaxies in the GIMIC simulations is dominated at late times by quasi-hydrostatic gas that has never been part of the ISM (and hence has never been ejected in a galactic fountain). It is therefore unlikely that outflows are the *dominant* metal transport mechanism at late times ($z \lesssim 1$) in GIMIC. There is, however, another mechanism by which the metals can be transported: convection. McCarthy et al. (2007) demonstrate that hydrostatic haloes grow in an inside–out fashion, such that the orbital kinetic energy associated with infalling gas is thermalized within the hot CGM of the main progenitor. The entropy of the infalling gas itself is largely unaffected, so it sinks to the halo centre and thus steadily convects the higher entropy and enriched gas, initially at the halo centre, to larger radii. It follows naturally that the metals synthesized earliest will reside furthest from the halo centre. Although some fraction of the hot CGM will flow inwards due to radiative cooling, a significant fraction of the gas has a long cooling time and will therefore convect as the halo is assembled. The dominance of this mechanism on time-scale grounds appears plausible; transporting metals at a distance of 250 kpc (the typical r_{200} at $z = 0$ for a galaxy in our simulation sample) in a period of 8 Gyr requires a net outflow velocity of only $\sim$30 km s^{-1}, roughly an order of magnitude lower than the characteristic velocity of SN-driven outflows as they emerge from the ISM.

4.4 Which mechanism dominates iron synthesis?

Having analysed the radial distribution of iron in the hot CGM, and the nature of its release into, and transport within, the hot CGM, we now turn to the *source* of the iron. We consider the synthesis by Type II SNe that occurs promptly ($\lesssim$30 Myr) after star formation episodes, and the synthesis by Type Ia SNe that is delayed with respect to star formation. As described by Wiersma et al. (2009b), the chemodynamics implementation adopted by GIMIC also accounts

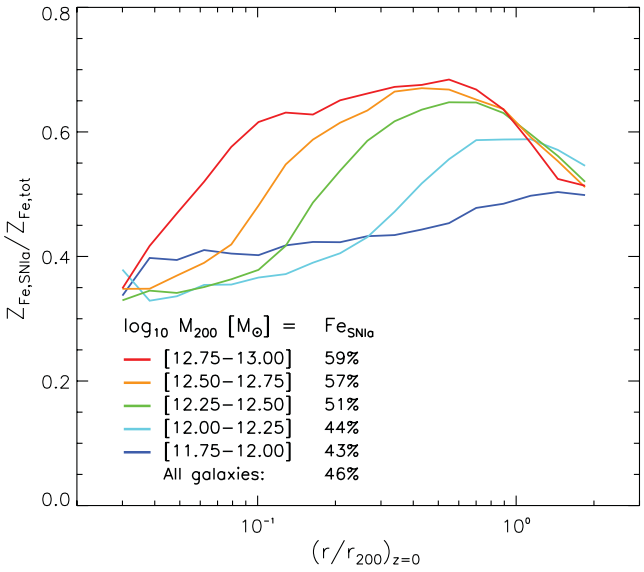

Figure 10. Spherically averaged radial profile of the mass fraction of iron within the hot CGM, synthesized by Type Ia SNe. The median iron mass fraction synthesized by Type Ia SNe within r_{200} for each halo mass bin is quoted next to the legend. Iron associated with the hot CGM of GIMIC galaxies is predominantly synthesized by Type Ia SNe; this is in spite of our adopted yields and Type Ia SN rates being such that an evolved ($t_{age} > 10^9$ Gyr) SSP with a Chabrier IMF tends to a near equipartition of iron production from Type II SNe and Ia SNe. We infer that iron synthesized by Type II SNe is preferentially (i) entrained in outflows and ejected from the system or (ii) locked up in secondary generations of stars.

for the fact that, whilst AGB stars do not synthesize iron, they do 'lock-up' significant quantities of iron when an SSP forms from pre-enriched gas. This iron is then gradually released by AGB envelope shedding on $\sim$Gyr time-scales.

In Fig. 10, we split the profiles presented in Fig. 6 into contributions from the two types of SNe, and plot the spherically averaged radial profile of the Type Ia-to-total iron mass fraction. The radially integrated ($0 < r < r_{200}$) iron mass fraction synthesized by Type Ia SNe is quoted for each halo mass bin in the legend. Both types of SN contribute at all radii to galaxies of all masses. The approximate equipartition of iron synthesized by each SN type follows from the behaviour of the stellar populations comprising the galaxy associated with each corona; adopting the yields and Type Ia SNe rates presented by Wiersma et al. (2009b), an evolved ($t_{age} \gtrsim 10^9$ yr) SSP with a Chabrier IMF tends to a broad equipartition of the iron mass fraction produced by each type of SN, particularly if the SSP has subsolar metallicity. However, we caution that this statement is sensitive to the assumed cosmic Type Ia rate[8] and the iron yield of Type Ia and II SNe.

There is, however, a mild but significant preference for iron synthesized by Type Ia SNe over that from Type II SNe in all but the least massive galaxies. We deduce two reasons why iron synthesized by Type II SNe is inhibited from residing in the hot CGM of galaxies at late cosmic epochs: first, the iron synthesized by Type II SNe is preferentially entrained in the energetic outflows that these events trigger, enabling a significant fraction of iron synthesized in

[8] The Type Ia SN delay function is ill constrained by theory and observation. The GIMIC simulations adopt an e-folding delay function with a characteristic time-scale of $\tau = 3.3$ Gyr.

this fashion to be ejected into the IGM at early epochs.[9] Secondly, because Type II SNe synthesize iron promptly, any iron from Type II SNe that is not ejected from the galaxy's potential is deposited into the dense ISM, where the enrichment products trigger efficient radiative cooling and readily become locked-up in secondary generations of stars. This is reflected in the abundance patterns of stars in the simulated galaxies: the fraction of Type II SN-synthesized iron in the stellar component of galaxies comprising our sample is typically 70–80 per cent (see also Font et al. 2011). However, we caution that this is likely a mild overestimate of the true fraction, since the inefficiency of feedback in the most massive galaxies comprising our sample will lead to too high a fraction of Type II SN-synthesized iron being unable to escape the confines of the ISM.

The trend with halo mass, such that the hot CGM of the most massive haloes is more strongly dominated by iron synthesized by Type Ia SNe ($Z_{\rm Fe,\,SNIa}/Z_{\rm Fe,\,tot} \sim 60$ per cent) can be interpreted in terms of the different star formation histories of the galaxies associated with these coronae. As shown in C09 (see fig. 6 therein), more massive galaxies in GIMIC complete a greater fraction of their star formation at high redshift, enabling a greater fraction of their stellar populations to evolve to the stage where a significant fraction of their ejected iron is contributed by Type Ia SNe.

The coronal iron mass fraction from Type Ia SNe in GIMIC is slightly lower than the 70–90 per cent estimated by HB06 for their sample of ellipticals, whose masses and X-ray luminosities are consistent with the most massive galaxies in the GIMIC sample. However, comparison of this result is not entirely instructive; we have not limited the GIMIC sample to 'elliptical' galaxies, and the limited X-ray spectroscopy available for disc galaxies with high star formation rates unsurprisingly indicate abundance patterns more consistent with Type II SN yields (Richings et al. 2010). Tang & Wang (2010) argue that the observable iron content of the hot CGM might in fact provide an unpresentative view of the total mass of iron synthesized by Type Ia SNe, because the iron is likely to be entrained in very hot, tenuous ejecta with a low specific soft X-ray emissivity and a large buoyancy that results in its rapid transport to large radii. Perhaps more importantly, however, SN nucleosynthesis yields remain uncertain at the factor of ∼2 level, and the cosmic Type Ia SN rate remains poorly constrained by both theory and observation. The simulations could remain entirely compatible with the cosmic Type Ia SN rate using double the adopted rate, and this would unquestionably improve the correspondence between the observed and predicted Type Ia iron fraction in the hot CGM. For this reason, we caution that comparison of the simulations with the currently available observational constraints is not particularly instructive.

5 SUMMARY AND DISCUSSION

We have investigated the enrichment of the hot CGM associated with $\sim L_\star$ ($10^{10} \lesssim M_\star \lesssim 10^{11.5}\,{\rm M}_\odot$) galaxies at $z = 0$, using the GIMIC simulations (C09). These simulations produce a large sample ($n = 617$) of well-resolved galaxies at $z = 0$, with a distribution of morphologies that broadly corresponds to that observed in the local Universe. We showed in Paper I that the simulations reproduce the observed $z = 0$ scalings of X-ray luminosity with K-band luminosity, star formation rate and disc rotation velocity. The simulations also reproduce the observed $z = 0$ stellar mass–rotation speed (or 'Tully–Fisher') and stellar mass–halo mass relations for $10^9 \lesssim M_\star/{\rm M}_\odot < 10^{10.5}$, but we caution that they still suffer from some overcooling for $M_\star \gtrsim 10^{11}\,{\rm M}_\odot$ (McCarthy et al. 2012b). The results from our simulations are summarized as follows.

(i) The hot CGM is dominated in a mass-weighted sense by metal-poor gas accreted from the IGM. Therefore, the iron abundance of the hot CGM, when integrating over all gas within the virial radius, is typically $\lesssim 0.1{\rm Z}_{\rm Fe,\,\odot}$.

(ii) Conversely, the X-ray emissivity of the hot CGM is dominated by line emission from collisionally excited metal ions that were synthesized in stars and transported out of the ISM. However, the excitation is caused by collisions with electrons; since heavy elements make only a small contribution to the free electron budget, these electrons are primarily sourced from the metal-poor gas accreted from the IGM.

(iii) The iron found in the hot CGM of galaxies in the GIMIC simulations at $z = 0$ was predominantly injected into gas that was, at the epoch of enrichment, already bound to the MMP of the galaxy, a process we term 'in situ' enrichment.

(iv) We find a clear correlation between the galactocentric radius of metals at $z = 0$ and the redshift at which they were synthesized, such that those synthesized at earlier cosmic epochs reside farther from the galaxy. Enrichment therefore proceeds in an 'inside–out' fashion, requiring the transport of metals from the central galaxy into the CGM. We speculate that this transport is dominated by SNe-driven winds at early times and by convection associated with the inside–out growth of the halo at later times, when the hot CGM is quasi-hydrostatic.

(v) Inside–out enrichment establishes a strong negative iron abundance gradient in the hot CGM. The spherically averaged radial profile of the iron abundance is typically supersolar at small radii ($\lesssim 0.05 r_{200}$), and rapidly declines to only a few per cent of the solar iron abundance at r_{200}, or to about 10 per cent of solar if the metallicity is weighted by the luminosity.

(vi) The strong negative metallicity gradient established by inside–out enrichment concentrates the majority of the metal ions associated with the hot CGM inside a relatively small radius. In contrast, following simple volumetric arguments, the majority of the mass of the hot CGM resides at large radius. Therefore, X-rays do not trace the distribution of the hot CGM in a simple fashion, rendering metallicity measurements of the hot CGM inferred from spatially unresolved X-ray spectroscopy biased towards the metal-rich gas close to the galaxy.

(vii) In addition, the sensitivity of plasma emissivity to the presence of metal ions induces a bias such that the luminosity-weighted metallicity of the hot CGM at a fixed radius is typically elevated with respect to its mass-weighted metallicity at the same radius. This induces a bias between luminosity- and mass-weighted metallicity measurements even when inferred from spatially resolved X-ray spectroscopy.

(viii) Both biases lead to abundance measures that are elevated with respect to the 'true', mass-weighted, measure. Therefore, despite exhibiting a typical iron abundance of $\lesssim 0.1{\rm Z}_{\rm Fe,\,\odot}$ at $z = 0$, the median $L_{\rm X}$-weighted iron abundance of the hot CGM is approximately ${\rm Z}_{\rm Fe,\,\odot}$, with a 2σ scatter of approximately one decade, across 5 decades in $L_{\rm X}$.

The simulations yield a correlation between $Z_{\rm Fe}$ and $L_{\rm X}$ that is weaker than implied by the combination of the HB06 and Ath07 data sets, but the recovered iron abundances are broadly consistent

[9] This is clearly a significant process, since the mass of gas ejected by a galaxy's stars over cosmic history is typically comparable to, or greater than, the mass of gas associated with the galaxy's potential at $z = 0$.

(within the 2σ scatter) with these data. The precise nature and origin of this relation is clearly an avenue of interesting future theoretical and observational enquiry. Similarly, the median core radius of our hot CGM profiles is larger than the core sizes inferred from the small number of measurements inferred from deep exposures of individual galaxies, or stacked profiles extracted from the *ROSAT* All-Sky Survey. As discussed in Section 2.7, we do not consider this a crucial shortcoming of our model, but note that the establishment of the surface density profile of circumgalactic gas remains an unresolved astrophysical problem that is well suited for study with the next generation of hydrodynamical simulations.

5.1 The interpretation of X-ray data in the context of galaxy formation theory

As remarked in Section 3.1, a central aim of this study is to ascertain whether the general picture of the formation of the hot CGM that is predicted by galaxy formation theory, and seen in cosmological hydrodynamical simulations, is compatible with constraints inferred from the most authoritative X-ray data sets presently available.

The GIMIC simulations follow the hierarchical assembly of the galaxies and include detailed phenomenological models for the formation of stars, the effects of SN-driven feedback, and the chemical evolution of evolving stellar populations. Whilst the simulations are known to produce inaccurate results in certain regimes (e.g. C09; McCarthy et al. 2012b) and necessarily offer an incomplete description of the formation of galaxies, they can be considered an authoritative test bed for confrontation with observational measurements, by virtue of the broad range of observable properties of local $\sim L_\star$ galaxies that they successfully reproduce (Font et al. 2011; McCarthy et al. 2012a,b).

In Paper I and in this study, we establish that $\sim L_\star$ galaxies in GIMIC broadly reproduce the key observed X-ray scaling relations of galaxies (i.e. with rotation velocity, stellar mass and star formation rate), and their inferred luminosity-weighted hot CGM iron abundance. Although the simulations are formally not fully consistent with the HB06 and Ath07 data sets, there is a broad correspondence between the two. This is a significant result, since the relatively high metallicity of the hot CGM of local galaxies has been perceived as a challenge to the prevailing model of galaxy formation, within which the hot CGM is assumed to form primarily via the accretion of metal-poor gas from the IGM throughout the assembly of the galaxy.

Our simulations indicate that the hot CGM of $L_\star$ galaxies is indeed dominated by gas accreted from the IGM. This picture appears similar to that advanced by simple analytic/semi-analytic models (e.g. White & Rees 1978; WF91), but in fact differs in two important ways. First, in contrast to the common assumption that the radial density profile of the hot CGM traces that of the underlying dark matter distribution, we showed in Paper I that SN-driven feedback lowers the normalization of the density profile and acts to soften the central cusp into a core by preferentially ejecting low-entropy gas from the halo centre. The reduction in central gas density lowers the luminosity of the halo by up to two orders of magnitude, because both line emission from collisional excitation and Bremsstrahlung radiation vary with the square of the gas density.

Secondly, as shown here, the dynamically complex and time-dependent enrichment of the hot CGM by the central galaxy, its satellites and external galaxies, establishes a strong negative radial metallicity gradient. This contrasts with the assumption of complete, uniform mixing within the cooling radius adopted by WF91. Since the emissivity of the gas is particularly sensitive to the presence of metal ions, this is an important difference that, like the density profile, has a marked effect on the luminosity and surface brightness profile of the hot CGM. Therefore, it is particularly encouraging that, in contrast to WF91, GIMIC broadly reproduces the luminosity *and* surface brightness profiles of galaxies in the local Universe.

This notwithstanding, the interpretation of diffuse X-ray emission associated with local $\sim L_\star$ galaxies remains controversial: the most common interpretation in the literature is that the emission associated with disc galaxies is a signature of hot plasma entrained in outflows driven by Type II SNe (e.g. Strickland et al. 2004; Wang 2005; Tüllmann et al. 2006; Rasmussen et al. 2009), whilst that associated with ellipticals is due to the heating of cold ISM gas by its interaction with the ejecta of intermediate age (AGB) stars and Type Ia SNe (e.g. Mathews 1990; Ciotti et al. 1991; Mathews & Brighenti 2003; Parriott & Bregman 2008). Whilst simple models based on these premises can lead to suggestive links between the optical and X-ray properties of galaxies, such models are, by construction, incomplete, because they start from idealized initial conditions, and are often unphysical, for example when assuming that galaxies are hydrodynamically decoupled from the IGM. Moreover, such models neglect, by construction, the role of the CGM as a reservoir of fuel for on-going star formation in galaxies. As we have argued in this study, a more complete model of galaxy formation is necessary to study the X-ray emission of the hot CGM, because it appears that the emission is the result of both accretion from the IGM and the transport of heavy elements from the ISM into the hot CGM.

The outstanding challenge is therefore to accommodate the interpretation of X-ray observations of galaxies within the context of modern hierarchical galaxy formation theory. As demonstrated in Paper I and in this study, many such observations are in fact reproduced by realistic, self-consistent hydrodynamical simulations that adopt cosmological initial conditions. For example, the broad correlations between $L_{\rm X}$ and $\dot{M}_\star$ (in disc galaxies) and $M_\star$ (in ellipticals) that provide the fundamental motivation for the idealized models described above, arise naturally in the GIMIC simulations because $L_{\rm X}$, $\dot{M}_\star$ and $M_\star$ all correlate with M_{200} for $\sim L_\star$ galaxies. It seems not unreasonable to expect, therefore, that improved modelling in this context will enable future simulations to reproduce a wide range of X-ray properties and scaling relations accurately. Moreover, as remarked in Paper I, the fundamental nature of the hot CGM of typical galaxies is, in principle, directly accessible via X-ray line diagnostics. Future X-ray observatories with the ability to obtain high-sensitivity spectroscopy at high spatial and spectral resolution therefore offer a direct means to identify the fraction of hot CGM entrained in outflows or residing in quasi-hydrostatic reservoirs. Observations with these facilities may thus verify or falsify the key role in the formation and evolution of galaxies that modern theoretical galaxy formation models assign to hot gaseous coronae.

ACKNOWLEDGEMENTS

IGM is supported by an STFC Advanced Fellowship. TT acknowledges the hospitality of the Kavli Institute for Theoretical Physics, Santa Barbara. CSF acknowledges a Royal Society Wolfson Research Merit Award. The simulations presented here were carried out by the Virgo Consortium for Cosmological Supercomputer Simulations using the HPCx facility at the Edinburgh Parallel Computing Centre (EPCC) as part of the EC's DEISA 'Extreme Computing Initiative', the Cosmology Machine at the Institute for Computational Cosmology of Durham University and on the Darwin facility at the University of Cambridge. This research was

supported in part by the National Science Foundation under Grant NSF PHY11-25915, the Netherlands Organization for Scientific Research (NWO), the Marie Curie Initial Training Network 'CosmoComp' (PITN-GA-2009-238536), the European Research Council under the European Union's Seventh Framework Programme (FP7/2007-2013) via grant agreement 278594-GasAroundGalaxies and the Advanced Investigator grant COSMIWAY and an STFC rolling grant awarded to the ICC.

REFERENCES

Abadi M. G., Moore B., Bower R. G., 1999, MNRAS, 308, 947
Anders E., Grevesse N., 1989, Geochim. Cosmochim. Acta, 53, 197 (AG89)
Anderson M. E., Bregman J. N., 2011, ApJ, 737, 22
Anderson M. E., Bregman J. N., Dai X., 2013, ApJ, 762, 106
Arimoto N., Matsushita K., Ishimaru Y., Ohashi T., Renzini A., 1997, ApJ, 477, 128
Asplund M., Grevesse N., Sauval A. J., 2005, in Barnes T. G., III, Bash F. N., eds, ASP Conf. Ser. Vol. 336, Cosmic Abundances as Records of Stellar Evolution and Nucleosynthesis. Astron. Soc. Pac., San Francisco, p. 25
Athey A. E., 2007, preprint (arXiv:0711.0395) (Ath07)
Bahé Y. M., McCarthy I. G., Crain R. A., Theuns T., 2012, MNRAS, 424, 1179
Benson A. J., 2010, Phys. Rep., 495, 33
Benson A. J., Bower R. G., Frenk C. S., White S. D. M., 2000, MNRAS, 314, 557
Boroson B., Kim D.-W., Fabbiano G., 2011, ApJ, 729, 12
Bower R. G., Benson A. J., Malbon R., Helly J. C., Frenk C. S., Baugh C. M., Cole S., Lacey C. G., 2006, MNRAS, 370, 645
Bregman J. N., Glassgold A. E., 1982, ApJ, 263, 564
Bregman J. N., Houck J. C., 1997, ApJ, 485, 159
Bregman J. N., Parriott J. R., 2009, ApJ, 699, 923
Bruzual G., Charlot S., 2003, MNRAS, 344, 1000
Buote D. A., 2002, ApJ, 574, L135
Buote D. A., Canizares C. R., 1994, ApJ, 427, 86
Buote D. A., Fabian A. C., 1998, MNRAS, 296, 977
Buote D. A., Lewis A. D., Brighenti F., Mathews W. G., 2003, ApJ, 595, 151
Chabrier G., 2003, PASP, 115, 763
Ciotti L., Ostriker J. P., 1997, ApJ, 487, L105
Ciotti L., Ostriker J. P., 2007, ApJ, 665, 1038
Ciotti L., D'Ercole A., Pellegrini S., Renzini A., 1991, ApJ, 376, 380
Cole S., Lacey C. G., Baugh C. M., Frenk C. S., 2000, MNRAS, 319, 168
Crain R. A. et al., 2009, MNRAS, 399, 1773 (C09)
Crain R. A., McCarthy I. G., Frenk C. S., Theuns T., Schaye J., 2010, MNRAS, 407, 1403 (Paper I)
Croton D. J. et al., 2006, MNRAS, 365, 11
Dai X., Anderson M. E., Bregman J. N., Miller J. M., 2012, ApJ, 755, 107
Dalla Vecchia C., Schaye J., 2008, MNRAS, 387, 1431
David L. P., Jones C., Forman W., Vargas I. M., Nulsen P., 2006, ApJ, 653, 207
Davis M., Efstathiou G., Frenk C. S., White S. D. M., 1985, ApJ, 292, 371
Dolag K., Borgani S., Murante G., Springel V., 2009, MNRAS, 399, 497
Dutton A. A., Conroy C., van den Bosch F. C., Prada F., More S., 2010, MNRAS, 407, 2
Fabbiano G., 1989, ARA&A, 27, 87
Fabbiano G., Juda J. Z., 1997, ApJ, 476, 666
Fang T., Buote D. A., Humphrey P. J., Canizares C. R., Zappacosta L., Maiolino R., Tagliaferri G., Gastaldello F., 2010, ApJ, 714, 1715
Ferland G. J., Korista K. T., Verner D. A., Ferguson J. W., Kingdon J. B., Verner E. M., 1998, PASP, 110, 761
Font A. S., McCarthy I. G., Crain R. A., Theuns T., Schaye J., Wiersma R. P. C., Dalla Vecchia C., 2011, MNRAS, 416, 2802
Forman W., Schwarz J., Jones C., Liller W., Fabian A. C., 1979, ApJ, 234, L27
Forman W., Jones C., Tucker W., 1985, ApJ, 293, 102
Foster C., Proctor R. N., Forbes D. A., Spolaor M., Hopkins P. F., Brodie J. P., 2009, MNRAS, 400, 2135
Gallazzi A., Charlot S., Brinchmann J., White S. D. M., 2006, MNRAS, 370, 1106
Gastaldello F., Molendi S., 2002, ApJ, 572, 160
Haardt F., Madau P., 2001, in Neumann D. M., Tran J. T. V., eds, Clusters of Galaxies and the High Redshift Universe Observed in X-rays. preprint (arXiv:astro-ph/0106018)
Haas M. R., Schaye J., Booth C. M., Dalla Vecchia C., Springel V., Theuns T., Wiersma R. P. C., 2012, preprint (arXiv:1211.1021)
Hatton S., Devriendt J. E. G., Ninin S., Bouchet F. R., Guiderdoni B., Vibert D., 2003, MNRAS, 343, 75
Heckman T. M., Armus L., Miley G. K., 1990, ApJS, 74, 833
Hodges-Kluck E. J., Bregman J. N., 2013, ApJ, 762, 12
Humphrey P. J., Buote D. A., 2006, ApJ, 639, 136 (HB06)
Humphrey P. J., Buote D. A., Canizares C. R., 2004, ApJ, 617, 1047
Jarrett T. H., Chester T., Cutri R., Schneider S. E., Huchra J. P., 2003, AJ, 125, 525
Jeltema T. E., Binder B., Mulchaey J. S., 2008, ApJ, 679, 1162
Kauffmann G., White S. D. M., Guiderdoni B., 1993, MNRAS, 264, 201
Kennicutt R. C., Jr, 1998, ARA&A, 36, 189
Kim D.-W., Fabbiano G., 2004, ApJ, 613, 933
Komatsu E. et al., 2011, ApJS, 192, 18
Lacey C., Cole S., 1994, MNRAS, 271, 676
Leitner S. N., Kravtsov A. V., 2011, ApJ, 734, 48
Lin Y.-T., Mohr J. J., 2004, ApJ, 617, 879
Li J.-T., Wang Q. D., 2013, MNRAS, 428, 2085
Li Z., Wang Q. D., Hameed S., 2007, MNRAS, 376, 960
Li Z. et al., 2011, ApJ, 730, 84
Loewenstein M., Mushotzky R. F., 1998, in Koyama K., Kitamoto S., Itoh M., eds, IAU Symp. 188, The Hot Universe. Kluwer, Dordrecht, p. 53
Martin D. C. et al., 2007, Nat, 448, 780
Mathews W. G., 1990, ApJ, 354, 468
Mathews W. G., Brighenti F., 2003, ARA&A, 41, 191
McCarthy I. G. et al., 2007, MNRAS, 376, 497
McCarthy I. G. et al., 2010, MNRAS, 406, 822
McCarthy I. G., Font A. S., Crain R. A., Deason A. J., Schaye J., Theuns T., 2012a, MNRAS, 420, 2245
McCarthy I. G., Schaye J., Font A. S., Theuns T., Frenk C. S., Crain R. A., Dalla Vecchia C., 2012b, MNRAS, 427, 379
Mitchell N. L., McCarthy I. G., Bower R. G., Theuns T., Crain R. A., 2009, MNRAS, 395, 180
Monaco P., Fontanot F., Taffoni G., 2007, MNRAS, 375, 1189
Mulchaey J. S., Jeltema T. E., 2010, ApJ, 715, L1
Nagai D., Lau E. T., 2011, ApJ, 731, L10
O'Sullivan E., Vrtilek J. M., Read A. M., David L. P., Ponman T. J., 2003, MNRAS, 346, 525
Okamoto T., Gao L., Theuns T., 2008, MNRAS, 390, 920
Owen R. A., Warwick R. S., 2009, MNRAS, 394, 1741
Parriott J. R., Bregman J. N., 2008, ApJ, 681, 1215
Pettini M., Shapley A. E., Steidel C. C., Cuby J.-G., Dickinson M., Moorwood A. F. M., Adelberger K. L., Giavalisco M., 2001, ApJ, 554, 981
Rasmussen J., Stevens I. R., Ponman T. J., 2004, MNRAS, 354, 259
Rasmussen J., Ponman T. J., Mulchaey J. S., Miles T. A., Raychaudhury S., 2006, MNRAS, 373, 653
Rasmussen J., Sommer-Larsen J., Pedersen K., Toft S., Benson A., Bower R. G., Grove L. F., 2009, ApJ, 697, 79
Read J. I., Hayfield T., 2012, MNRAS, 422, 3037
Renzini A., 1997, ApJ, 488, 35
Richings A. J., Fabbiano G., Wang J., Roberts T. P., 2010, ApJ, 723, 1375
Schaye J., Dalla Vecchia C., 2008, MNRAS, 383, 1210
Schaye J., Carswell R. F., Kim T.-S., 2007, MNRAS, 379, 1169
Schaye J. et al., 2010, MNRAS, 402, 1536
Shen S., Wadsley J., Stinson G., 2010, MNRAS, 407, 1581
Shen S., Madau P., Aguirre A., Guedes J., Mayer L., Wadsley J., 2012, ApJ, 760, 50

Simionescu A. et al., 2011, Sci, 331, 1576
Smith R. K., Brickhouse N. S., Liedahl D. A., Raymond J. C., 2001, ApJ, 556, L91
Somerville R. S., Hopkins P. F., Cox T. J., Robertson B. E., Hernquist L., 2008, MNRAS, 391, 481
Spolaor M., Kobayashi C., Forbes D. A., Couch W. J., Hau G. K. T., 2010, MNRAS, 408, 272
Springel V., 2005, MNRAS, 364, 1105
Springel V., White S. D. M., Tormen G., Kauffmann G., 2001, MNRAS, 328, 726
Springel V. et al., 2005, Nat, 435, 629
Springel V. et al., 2008, MNRAS, 391, 1685
Strickland D. K., Heckman T. M., Colbert E. J. M., Hoopes C. G., Weaver K. A., 2004, ApJS, 151, 193
Sun M., Jones C., Forman W., Vikhlinin A., Donahue M., Voit M., 2007, ApJ, 657, 197
Sun M., Voit G. M., Donahue M., Jones C., Forman W., Vikhlinin A., 2009, ApJ, 693, 1142
Tamura T., Kaastra J. S., Makishima K., Takahashi I., 2003, A&A, 399, 497
Tang S., Wang Q. D., 2010, MNRAS, 408, 1011
Terlevich A. I., Forbes D. A., 2002, MNRAS, 330, 547
Trager S. C., Faber S. M., Worthey G., González J. J., 2000a, AJ, 119, 1645
Trager S. C., Faber S. M., Worthey G., González J. J., 2000b, AJ, 120, 165
Trinchieri G., Kim D.-W., Fabbiano G., Canizares C. R. C., 1994, ApJ, 428, 555
Tüllmann R., Pietsch W., Rossa J., Breitschwerdt D., Dettmar R.-J., 2006, A&A, 448, 43
van de Voort F., Schaye J., 2013, MNRAS, 430, 2688
Veilleux S., Cecil G., Bland-Hawthorn J., 2005, ARA&A, 43, 769
Vogler A., Pietsch W., Kahabka P., 1995, Adv. Space Res., 16, 139
Wadsley J. W., Veeravalli G., Couchman H. M. P., 2008, MNRAS, 387, 427
Wang Q. D., 2005, in Braun R., ed., ASP Conf. Ser. Vol. 331, Extra-Planar Gas. Astron. Soc. Pac., San Francisco, p. 329
Wareing C. J., O'Brien T. J., Zijlstra A. A., Kwitter K. B., Irwin J., Wright N., Greimel R., Drew J. E., 2006, MNRAS, 366, 387
White S. D. M., Frenk C. S., 1991, ApJ, 379, 52 (WF91)
White S. D. M., Rees M. J., 1978, MNRAS, 183, 341
Wiersma R. P. C., Schaye J., Smith B. D., 2009a, MNRAS, 393, 99
Wiersma R. P. C., Schaye J., Theuns T., Dalla Vecchia C., Tornatore L., 2009b, MNRAS, 399, 574
Wiersma R. P. C., Schaye J., Dalla Vecchia C., Booth C. M., Theuns T., Aguirre A., 2010, MNRAS, 409, 132
Wiersma R. P. C., Schaye J., Theuns T., 2011, MNRAS, 415, 353
Xu H. et al., 2002, ApJ, 579, 600

APPENDIX A: NUMERICAL CONVERGENCE

We next consider the effects of numerical resolution. Focusing on the $Z_{\rm Fe}$–$L_{\rm X}$ scaling relations, we follow the methodology adopted by C09, Font et al. (2011) and McCarthy et al. (2012a), and compare the $Z_{\rm Fe}$–$L_{\rm X}$ relation derived from the intermediate-resolution simulations with results from the high-resolution realization of the -2σ GIMIC region. The high-resolution realizations have a factor of 8 better mass resolution than the intermediate-resolution realizations (see Section 2.1).

In Fig. A1, we compare the mass-weighted (left) and $L_{\rm X}$-weighted (right) metallicity-luminosity scaling of the 74 galaxies satisfying our selection criteria (see Section 2.3) in the high-resolution -2σ region (black points), with the median and scatter derived from the sample of 617 galaxies in all five intermediate-resolution regions (red hatching). The correspondence between the high- and intermediate-resolution samples is good, indicating that the $Z_{\rm Fe}$–$L_{\rm X}$ relations (both mass-weighted and $L_{\rm X}$-weighted) are numerically converged in the intermediate-resolution simulations.

APPENDIX B: METALLICITY SMOOTHING

In Section 2.6, we discussed the lack of implicit scalar quantity diffusion in SPH, and the consequent suppression of metal mixing that unavoidably results from the finite sampling of the fluid. Here, we suppress the effects of suppressed mixing by kernel-weighted averaging element abundances over a given particle's SPH neighbours when computing cooling rates, radiative luminosities and coronal metallicities.

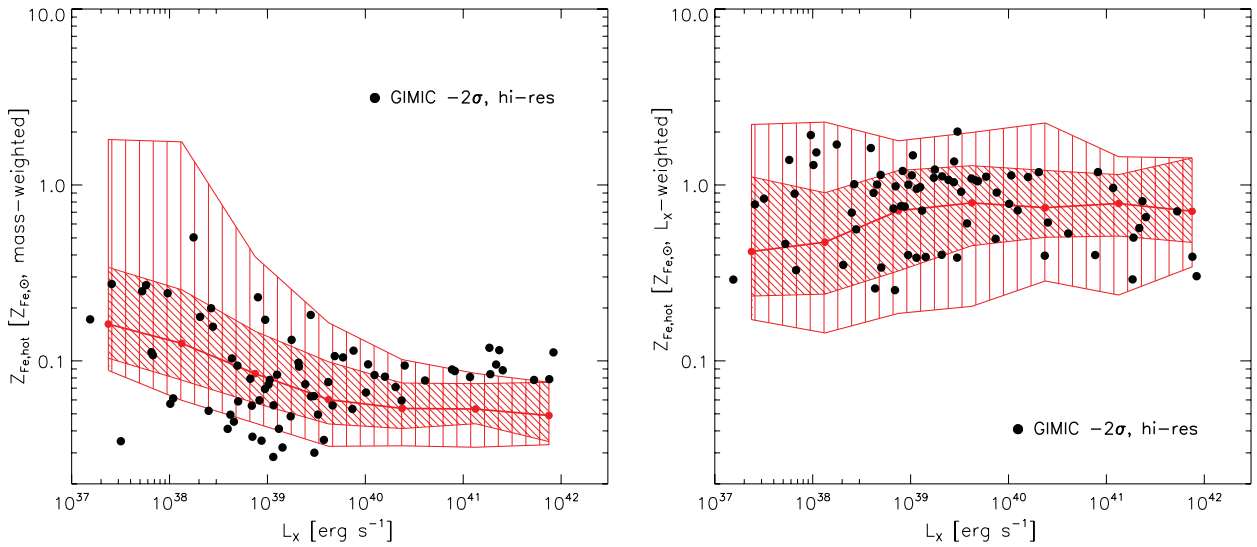

Figure A1. The mass-weighted (left) and luminosity-weighted (right) $Z_{\rm Fe}$–$L_{\rm X}$ relations defined by the 74 galaxies satisfying our selection criteria in the high-resolution -2σ GIMIC simulation, overplotted on the median and (1, 2)σ scatter (hatched regions) defined by the sample of 617 galaxies drawn from all five intermediate-resolution simulations. The relations described by the intermediate- and high-resolution simulations are numerically converged.

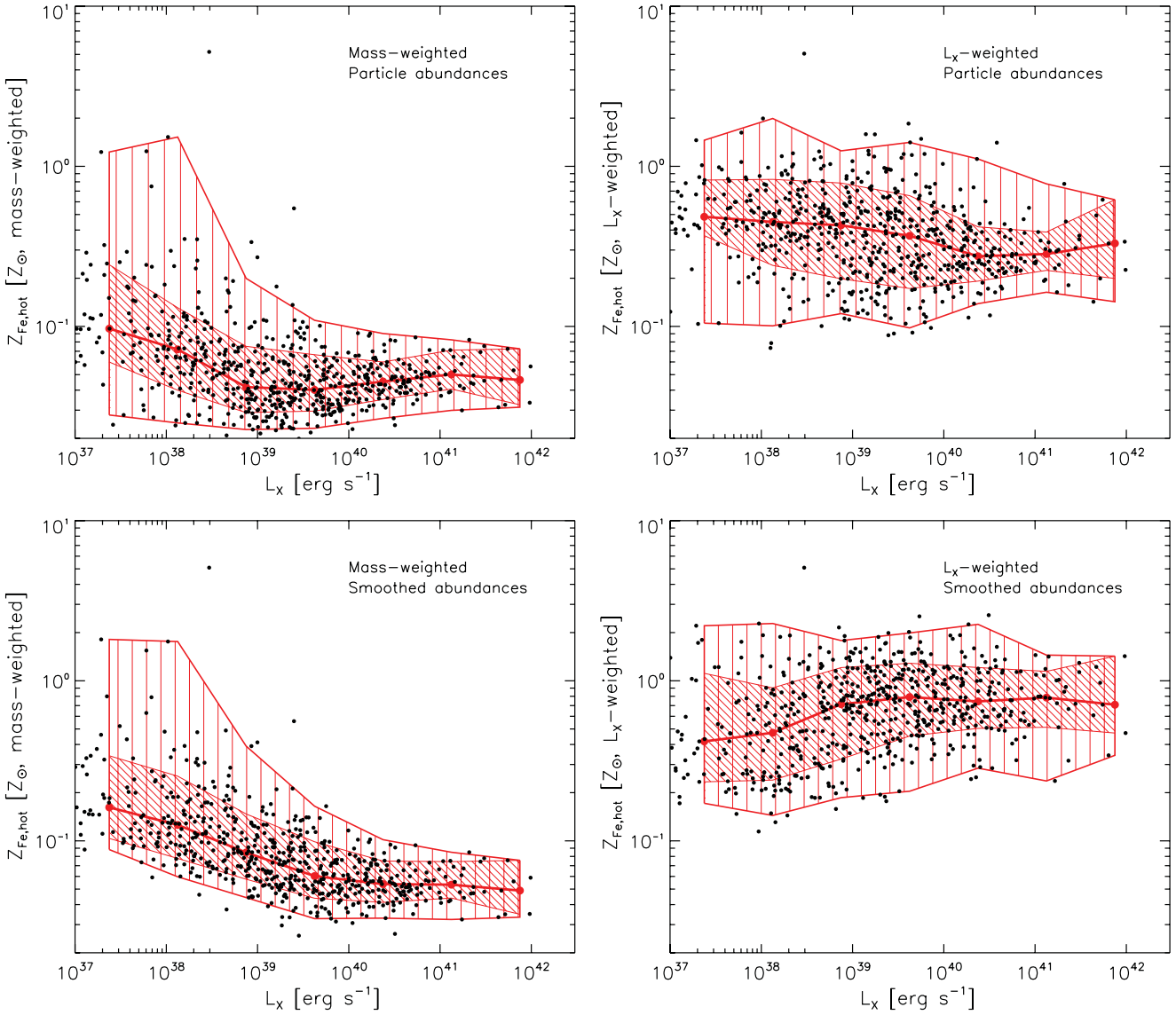

Figure B1. Comparison of the mass-weighted (left-hand column) and $L_{\rm X}$-weighted (right-hand column) $Z_{\rm Fe}$–$L_{\rm X}$ relations recovered when adopting particle-based (top row) and smoothed (bottom row) element abundances. The different abundance measures produce differences in the mass-weighted relation only for low-luminosity systems that are poorly resolved. The luminosity-weighted relation exhibits differences for all systems probed here, but only at the factor of $\lesssim$3 level. Our conclusions are therefore insensitive to the use of the particle-based or smoothed element abundances when measuring coronal metallicities and computing particle X-ray luminosities.

This smoothing procedure induces only a small error in the resulting total metal mass (see Wiersma et al. 2009b),[10] but does have the potential to bias the recovered metallicity of hot circumgalactic particles, because smoothed metallicities are computed using all SPH neighbour particles, irrespective of their thermal state. The smoothed element abundances of hot particles close to the disc–corona interface are therefore computed from both cold (i.e. ISM) and hot (coronal) particles. The maximum possible effect of such a potential bias can be determined by recomputing the metallicity and X-ray luminosity of each galaxy's hot CGM, using particle abundances instead of the SPH-smoothed abundances.

[10] Strict conservation is not achieved because metals are distributed with a gather, rather than scatter, approach.

In Fig. B1, we compare the mass-weighted (left-hand column) and $L_{\rm X}$-weighted (right-hand column) $Z_{\rm Fe}$–$L_{\rm X}$ relations derived from the particle (top row) and smoothed (bottom row) abundances. As in previous figures, each dot represents a simulated galaxy, whilst the densely and sparsely hatched regions represent the 1σ and 2σ scatter, respectively.

It is clear that the total X-ray luminosity is insensitive to metal mixing uncertainties, since no systematic shift in $L_{\rm X}$ is observed. Similarly, the recovered mass-weighted metallicity is little changed in well-resolved coronae, since the smoothing broadly conserves metal mass. In the lowest luminosity systems, which are less well resolved than more massive counterparts, the coronal metallicity derived from the particle abundances is lower by a factor of $\lesssim$2, indicating that the degree of biasing caused by the smoothing of metals from cold ISM is small. It is, for example, smaller than the uncertainty in our adopted metal yields.

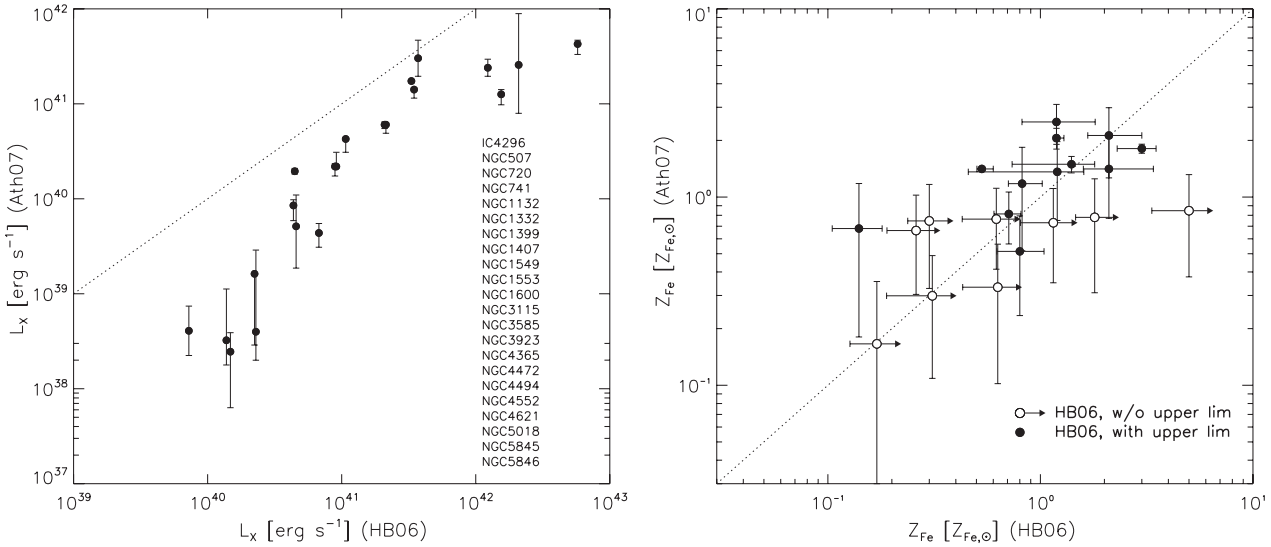

Figure C1. The X-ray luminosity (left) and iron abundance (right) inferred by Ath07 as a function of that inferred by HB06, for the 22 galaxies present in both samples. The names of these galaxies are listed in the left-hand panel. Luminosity uncertainties are quoted only by Ath07. As in Fig. 3, we plot galaxies from HB06 with no formal upper limit on Z_{Fe} as the open circles with arrows towards higher values. Iron abundances inferred by both studies are mostly consistent, and follow the 1:1 trend, albeit with significant scatter. Ath07 report systematically lower luminosities than HB06 for the lowest luminosity galaxies. Our conclusions are, however, robust to these uncertainties.

The effect on the luminosity-weighted metallicity is slightly larger: metallicities derived from particle abundances are lower by a factor of $\lesssim$3. In contrast to the mass-weighted quantities, this result is relatively insensitive to the coronal luminosity, because the most luminous particles are always those closest to the disc–corona interface. Therefore, the extent of the largest possible bias resulting from our use of smoothed abundances is only marginally greater than the intrinsic uncertainty in our adopted metal yields, and does not impact upon our conclusions.

APPENDIX C: PROPERTIES INFERRED BY HB06 AND ATH07 FROM *CHANDRA* SPECTROSCOPY

As described in Section 3.1, we use the HB06 sample as our fiducial sample and supplement this with unique galaxies from the Ath07 sample, since these extend to lower X-ray luminosity. It is interesting briefly to examine the correspondence between the values of Z_{Fe} and L_X recovered by both studies from the archival *Chandra* spectroscopy for the 22 galaxies that were included in both samples, in order to assess the impact of systematic uncertainties.

In Fig. C1, we plot the soft X-ray luminosity (left) and the iron abundance (right) of hot circumglactic gas, reported by Ath07, as a function of that reported by HB06. In each case, the 1:1 correspondence is shown as a dotted line. Ath07 report systematically lower luminosities, with the faintest and brightest galaxies differing by over a decade in L_X, whilst intermediate luminosity galaxies ($L_X \sim 10^{42}$ erg s^{-1}) are offset by $\sim$0.5 dex. The inferred metallicities show no such systematic offset, and broadly trace the 1:1 locus, albeit with broad scatter.

The differences between the measurements highlight the difficulty of reducing X-ray spectra, and fitting plasma models to these data to infer luminosities and metallicities. However, the uncertainties apparent here do not affect our conclusions: the inferred metallicities are not systematically offset, whilst the application of a systematic offset to the luminosities reported by either HB06 or Ath07 would merely require the data to be translated along the *x*-axis in the left-hand panel of Fig. 3. Since the simulated galaxies exhibit a flat Z_{Fe}–L_X relation, such a translation would leave the simulations entirely compatible with the data.

This paper has been typeset from a TEX/LATEX file prepared by the author.